

Antenna Selection With Beam Squint Compensation for Integrated Sensing and Communications

Ahmet M. Elbir, *Senior Member, IEEE*, Asmaa Abdallah, *Member, IEEE*,
Abdulkadir Celik, *Senior Member, IEEE*, and Ahmed M. Eltawil, *Senior Member, IEEE*

Abstract—Next-generation wireless networks strive for higher communication rates, ultra-low latency, seamless connectivity, and high-resolution sensing capabilities. To meet these demands, terahertz (THz)-band signal processing is envisioned as a key technology offering wide bandwidth and sub-millimeter wavelength. Furthermore, THz integrated sensing and communications (ISAC) paradigm has emerged jointly access spectrum and reduced hardware costs through a unified platform. To address the challenges in THz propagation, THz-ISAC systems employ extremely large antenna arrays to improve the beamforming gain for communications with high data rates and sensing with high resolution. However, the cost and power consumption of implementing fully digital beamformers are prohibitive. While hybrid analog/digital beamforming can be a potential solution, the use of subcarrier-independent analog beamformers leads to the beam-squint phenomenon where different subcarriers observe distinct directions because of adopting the same analog beamformer across all subcarriers. In this paper, we develop a sparse array architecture for THz-ISAC with hybrid beamforming to provide a cost-effective solution. We analyze the antenna selection problem under beam-squint influence and introduce a manifold optimization approach for hybrid beamforming design. To reduce computational and memory costs, we propose novel algorithms leveraging grouped subarrays, quantized performance metrics, and sequential optimization. These approaches yield a significant reduction in the number of possible subarray configurations, which enables us to devise a neural network with classification model to accurately perform antenna selection. Numerical simulations show that the proposed approach exhibits up to 95% lower complexity for large antenna arrays while maintaining satisfactory communications with approximately 6% loss in the achievable rate.

Index Terms—Antenna selection, integrated sensing and communications, massive MIMO, terahertz, machine learning.

I. INTRODUCTION

THE escalating demand for wireless communications and radar systems has engendered a scarcity of available frequency bands, resulting in pervasive overcrowding and spectrum congestion [1, 2]. To combat this predicament, specialized techniques such as carrier aggregation and spectrum stitching have been harnessed in communications systems to efficiently utilize the spectrum [3]. However, the application of these techniques to radar systems poses formidable challenges in achieving meticulous phase synchronization [2]. Consequently, it is crucial to cultivate approaches that enable the simultaneous and opportunistic operation within the same

frequency bands, thus benefiting from both radar sensing and communications functionalities on a shared hardware platform. Therefore, there has been a significant interest focused on the development of strategies for integrated sensing and communications (ISAC) setups, aiming to jointly access the scarce spectrum in a mutually advantageous manner [4–6].

The earlier ISAC designs utilize distinct hardware platforms to carry out sensing and communications (S&C) functions within the same frequency bands. These designs employed various techniques to mitigate interference between the two domains. Broadly, the ISAC systems are categorized into two primary groups: radar-communications coexistence (RCC) and dual-functional radar-communications (DFRC) [2, 7]. While RCC focuses on managing interference and sharing resources between S&C tasks, enabling them to operate without significant mutual disruption, DFRC aims to consolidate both tasks onto a common platform, resulting in the convergence of ISAC design [4, 7]. The necessity for a unified hardware platform becomes increasingly imperative as the integration of communications and sensing capabilities continues to advance in various applications, such as vehicle-to-everything (V2X) communication, indoor localization, radio frequency (RF) tagging, extended/virtual reality, unmanned aerial vehicles (UAVs), and intelligent reflecting surfaces (IRSs) [6, 8–15]. The terahertz (THz) band (0.1 – 10 THz) has emerged as a promising technology to meet the sixth-generation (6G) wireless networks’ ambitious performance goals on enhanced mobile broadband (eMBB), massive machine-type communication (mMTC), and ultra-reliable low-latency communication (URLLC) [4, 11]. As the spectrum allocation beyond 100 GHz is underway, there is a surge of research activity in ISAC to develop system architectures that can simultaneously achieve high-resolution sensing and high data rate communication at both upper millimeter-wave (mmWave) frequencies and low THz frequencies [2, 4, 6, 8].

To meet the aforementioned diverse functionalities, the THz-ISAC system encounters several notable challenges, including but not limited to severe path loss resulting from spreading loss and molecular absorption, limited transmission range, and beam-squint caused by the ultra-wide bandwidth [4, 16]. These challenges significantly impact the performance of both S&C aspects through: 1) the high path loss leads to extremely low signal-to-noise ratio (SNR) at both radar and communications receivers; 2) the Doppler shift accompanied by high range sidelobes can trigger false alarms during sensing and introduce inter-carrier interference to the communication systems, and 3) the beam-squint effects cause deviations

A. M. Elbir, A. Abdallah, A. Celik and A. M. Eltawil are with King Abdullah University of Science and Technology, Thuwal 23955, Saudi Arabia (e-mail: ahmetmelbir@ieee.org, asmaa.abdallah@kaust.edu.sa, abdulka-dir.celik@kaust.edu.sa, ahmed.eltawil@kaust.edu.sa).

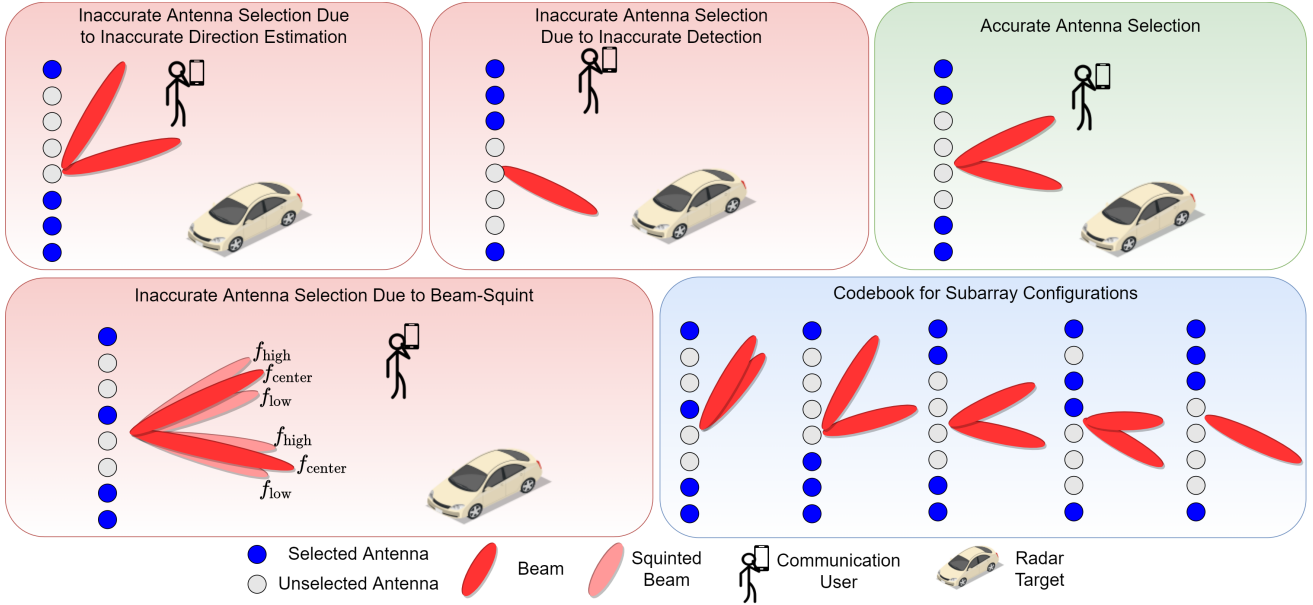


Fig. 1. Antenna selection for various scenarios. A codebook of subarray configurations is given to accurately select the antennas. Inaccurate antenna selection emerges due to failed direction estimation, misdetection and beam-squint which causes the generated beams point to different directions across the subcarriers.

in the generated beams across different subcarriers, thereby diminishing the array gain and subsequently reducing the spectral efficiency (SE) for communication and the accuracy of direction-finding (DF) for sensing purposes.

To address these challenges, the implementation of ISAC concept in massive multiple-input multiple-output (MIMO) systems necessitates large antenna arrays at the base station (BS) to achieve significant beamforming gain [3, 17, 18]. Conversely, massive MIMO systems are also designed with fewer radio frequency (RF) chains to minimize hardware costs. This creates a motivation to develop an efficient ISAC design that carefully balances the system complexity in dealing with challenges such as path loss and beam-squint, while considering the cost implications associated with large arrays. To reduce this cost, antenna selection is an attractive solution that can select only a high quality subset of antennas to connect the reduced number of RF chains [19–22]. By maintaining a large portion of the same array aperture with fewer antenna elements connected to limited number of RF chains, antenna selection-based systems can achieve a comparable resolution while reducing size, weight, and power-cost (SWAP-C) by utilizing antenna selection diversity [23]. Nonetheless, removing an element from the antenna array raises the sidelobe levels in the antenna beam pattern. This may introduce the ambiguity of resolving target directions in radar systems and the larger interference to other users in communications. Thus, antenna selection in ISAC systems is even more challenging than communications-only and sensing-only systems, and it should take into account the prior information and the constraints related to both S&C functionalities.

To strike a good balance between SE and system complexity, massive MIMO systems employ wideband signal processing, wherein the transceiver architecture is composed of subcarrier-dependent (SD) baseband and subcarrier-

independent (SI) analog beamformers. While the SD baseband processing can be carried out on a single hardware platform, the realization of the analog beamformer requires the implementation of phase shifter networks whose size is proportional to the number of subcarriers. As a result, the SI design enjoys a significant hardware simplicity and cost efficiency compared to the SD analog beamformers [24]. When the analog beamformers are SI, its design is only constrained by a single (sub-)carrier frequency [25, 26]. Therefore, the beams generated across the subcarriers point to different directions causing beam-squint phenomenon [27, 28]. The existing techniques to compensate for the impact of beam-squint mostly employ additional hardware components, e.g., time-delayer (TD) networks [29, 30] and SD phase shifter networks [24] to virtually realize SD analog beamformers. However, these approaches are inefficient in terms of cost and power [30, 31]. Beam-squint also occurs in transceivers with antenna selection. Fig. 1 illustrates accurate and inaccurate antenna selection configurations for various ISAC scenarios. Although a codebook of selected antennas for different scenarios is available, it should take into account the impact of beam-squint. Otherwise, the squinted beams from the subarray point to different directions may cause inaccurate target detection/estimation for sensing as well as a significant loss in communications rate.

A. Related Work

Recent research includes several works separately on beam-squint compensation [24, 29, 30, 32, 33] and sparse array design for communications [19, 20, 22], sensing [34] as well as ISAC [22, 35–38]. However, the impact of beam-squint on sparse array design has not been considered in the relevant literature. Because of beam-squint, the performance metric, e.g., SE [19, 20, 39], channel gain [40] and Cramér-Rao bound (CRB) [34–36, 41], receive antenna power [42], becomes

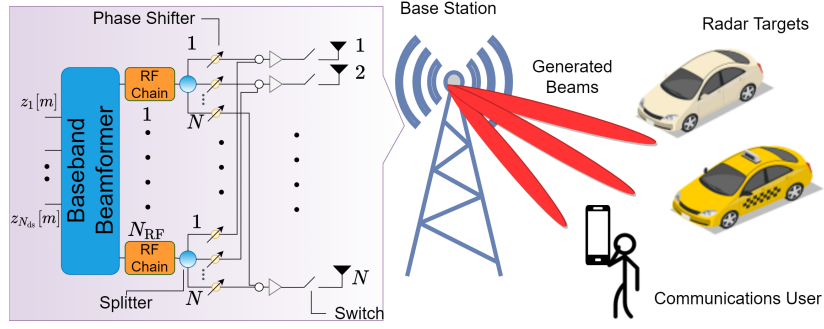


Fig. 2. ISAC transmitter architecture with hybrid beamforming and antenna selection.

miscalculated during antenna selection. Specifically, beam-squint corrupts the array gain and it causes false (deviated) peaks in the spatial domain due to the angular deviations in the generated beams. Therefore, if beam-squint is not compensated properly, the subarray corresponding to the false peaks may differ than that of the optimum subarray.

Without examining the impact of beam-squint, antenna selection in ISAC scenario is considered in several works [22, 35–38]. In particular, antenna selection is performed in [35] and [36] via employing the CRB of the target parameter estimation as performance metric. In [37] and [22], the authors introduce various ISAC architectures with sparse arrays for single-user configuration. Also, in [38], a multi-user, single-target scenario is considered, wherein a fully digital beamforming approach is proposed. Different from the aforementioned model-based techniques, a deep learning (DL)-based approach is proposed in [43], wherein analog-only beamforming for transmit antenna selection in ISAC scenario is considered. Furthermore, most of the antenna selection strategies for ISAC examine whether only analog [43] or digital [22, 35, 37, 38] beamformer design without considering hybrid analog/digital beamforming. Although a CRB-based antenna selection and hybrid beamforming is considered in [36], the analog and digital beamformers are not optimized. Besides, DL-based joint hybrid beamforming and antenna selection is studied in various recent works with different settings, e.g., unsupervised learning [44], online learning [45], quantized learning model [19], and graph learning models [46]. However, these works are limited to communications-only scenario and do not consider the impact of beam-squint in wideband systems.

B. Contributions

In this work, we investigate the impact of beam-squint on antenna selection for THz-ISAC hybrid beamforming. The computational complexity of the antenna selection problem is high due to its combinatorial nature, which is addressed by proposed low complexity heuristic solutions that reduce the number of subarray candidates. The performance metric for designing the ISAC hybrid beamformers is the SE of the selected subarray. The main contributions of this work are summarized as follows:

- To design the ISAC hybrid beamformers, we propose a manifold optimization-based approach that incorporates beam-squint compensation (BSC). Unlike recent works on hybrid beamforming with manifold optimization, our approach incorporates wideband processing with BSC.
- We devise low complexity algorithms for antenna selection. In particular, a grouped subarray selection (GSS) approach is proposed, wherein the entire array is divided into distinct, non-overlapping groups, allowing us to select antennas in groups rather than individually, thereby significantly reducing the number of potential subarray configurations. Additionally, we develop a sequential search algorithm to minimize memory requirements during the implementation of antenna selection.
- By reducing the number of potential subarray configurations, we formulate the antenna selection problem as a classification problem. We develop a learning model with convolutional neural network (CNN) architecture that combines communications and sensing data to efficiently determine the subarray configuration. The CNN model takes the combined communications data (channel matrix) and sensing data (target response vectors) as input. Through training, the CNN model generates the optimal subarray configuration as the output.
- We examine the impact of beam-squint and subarray configuration in terms of SE of the overall system. In particular, we show, via both theoretical analysis and numerical experiments, that the highest performance can only be achieved if the best subarray is selected and the beam-squint is completely compensated.

In the remainder of the paper, we present the THz-ISAC architecture with communications and sensing signal model in Section II. Next, we introduce the proposed joint antenna selection and hybrid beamforming approach in Section III. After presenting various experimental results in Section IV, the paper is finalized with conclusions in Section V.

Notation: Throughout the paper, we use $(\cdot)^T$, $(\cdot)^H$ and $(\cdot)^*$ for transpose and conjugate transpose and complex conjugate operations, respectively. For a matrix \mathbf{A} and vector \mathbf{a} ; $[\mathbf{A}]_{i,j}$, $[\mathbf{A}]_k$ and $[\mathbf{a}]_l$ correspond to the (i, j) -th entry, k -th column and l -th entry, respectively. Furthermore, $\text{vec}\{\mathbf{A}\}$ denotes the vectorized form of \mathbf{A} with $\mathbf{A} = \text{vec}^{-1}\{\text{vec}\{\mathbf{A}\}\}$. $\mathbb{E}\{\cdot\}$ represent the flooring and expectation operations, respectively.

The binomial coefficient is defined as $\binom{n}{k} = \frac{n!}{k!(n-k)!}$. An $N \times N$ identity matrix is represented by \mathbf{I}_N . We denote $\|\cdot\|_0$, $\|\cdot\|_2$ and $\|\cdot\|_{\mathcal{F}}$ as the ℓ_0 -norm, ℓ_2 -norm and Frobenious norms, respectively. $\zeta(a) = \frac{\sin N\pi a}{N \sin \pi a}$ is the Dirichlet sinc function, and $|\mathbf{A}|$ denotes the determinant of \mathbf{A} . \odot and \otimes denote the element-wise Hadamard and Kronecker products, respectively. The Riemannian and Euclidean gradients are represented by $\nabla_{\mathcal{R}}$ and ∇ , respectively.

II. SYSTEM MODEL

Consider a wideband ISAC system with hybrid beamforming architecture driven by N_{RF} RF chains and M subcarriers as shown in Fig. 2. The BS employs N antennas and aims to simultaneously generate multiple beams towards T targets and a single communications user with N' antennas, for which N_{ds} data symbols are transmitted. The BS performs an antenna selection scheme to employ a sparse array of size K out of N^{12} . Denoted by $z_i[m]$, $i = 1, \dots, N_{\text{ds}}$, the transmitted data symbols at the m -th subcarrier ($m = \mathcal{M} = \{1, \dots, M\}$), the BS applies the SD digital beamformer $\mathbf{F}_{\text{BB}}[m] \in \mathbb{C}^{N_{\text{RF}} \times N_{\text{ds}}}$. Using the K -element sparse array, the BS applies the SI analog beamformer, $\mathbf{F}_{\text{RF}} \in \mathbb{C}^{K \times N_{\text{RF}}}$ which is realized with fully-connected phase shifter network³. Due to phase-only processing in the phase shifters, the entries of the analog beamformer have the constant modulus property, i.e., $|\mathbf{F}_{\text{RF}}[i,j]| = 1/\sqrt{K}$ for $i = 1, \dots, K$ and $j = 1, \dots, N_{\text{RF}}$. Then, the $K \times 1$ transmitted signal at the m -th subcarrier becomes

$$\mathbf{g}[m] = \mathbf{F}_{\text{RF}} \mathbf{F}_{\text{BB}}[m] \mathbf{z}[m], \quad (1)$$

where $\mathbf{z}[m] = [z_1[m], \dots, z_{N_{\text{ds}}}[m]]^T$, and $\mathbb{E}\{\mathbf{z}[m] \mathbf{z}^H[m]\} = \frac{1}{N_{\text{ds}}} \mathbf{I}_{N_{\text{ds}}}$.

A. Communications Model

Denote the downlink THz channel matrix between the BS and the communications user as $\bar{\mathbf{H}}[m] \in \mathbb{C}^{N' \times N}$. Then, the channel matrix with selected antennas is

$$\mathbf{H}[m] = \bar{\mathbf{H}}[m] \mathbf{Q}, \quad (2)$$

where $\mathbf{Q} \in \{0, 1\}^{N \times K}$ is the selection matrix. Specifically, for the (n, k) -th element of \mathbf{Q} , $[\mathbf{Q}]_{n,k} = 1$ represents that the n -th transmit antenna is the k -th selected antenna for $n \in \{1, \dots, N\}$ and $k \in \{1, \dots, K\}$. Then, the $N' \times 1$ received signal vector at the user becomes

$$\begin{aligned} \mathbf{y}[m] &= \bar{\mathbf{H}}[m] \mathbf{Q} \mathbf{g}[m] + \mathbf{n}[m] \\ &= \mathbf{H}[m] \mathbf{F}_{\text{RF}} \mathbf{F}_{\text{BB}}[m] \mathbf{z}[m] + \mathbf{n}[m], \end{aligned} \quad (3)$$

where $\mathbf{n}[m] \in \mathbb{C}^{N'}$ denotes the temporally and spatially white additive zero-mean Gaussian noise vector with variance σ^2 .

¹We note here that the selected K antennas are optimized and dedicated to a pair of communications user and radar target for a particular coherence time. The remaining $N - K$ antennas can concurrently be used for another ISAC scenario involving a different user-target pairs available in the network.

²The number of selected antennas K should satisfy $T + L \leq N_{\text{RF}} \leq K \leq N$ to simultaneously generate $T + L$ beams towards T targets and L user path directions.

³While there are works on partially-connected or subarrayed phase shifter network architectures with [19, 20] or without [6, 47] antenna selection, the proposed approach can be easily extended to these architectures via simple modifications in the selection matrix.

1) *THz Channel*: Channel modeling in THz band has been a challenging task largely because of the lack of realistic measurement campaigns [48–50]. In [49, 50], it is shown that a single dominant line-of-sight (LoS) path with a few non-LoS (NLoS) multipath components survive at the receiver in outdoor scenarios for sub-THz frequencies [51]. In a general scenario, e.g., indoor, multipath channels can also arise, the gains of LoS and NLoS paths are comparable [16, 52, 53]. Therefore, we assume a general scenario, wherein the THz channel matrix $\bar{\mathbf{H}}[m]$ includes the contribution of L multipath scatterers as

$$\bar{\mathbf{H}}[m] = \sqrt{\frac{N'N}{L}} \sum_{l=1}^L \alpha_{l,m} \mathbf{a}'(\phi_l) \mathbf{a}^H(\theta_l), \quad (4)$$

where $\alpha_{l,m} \in \mathbb{C}$ denotes the gain of the l -th path, and it can be defined for a LoS path as

$$\alpha_{l,m}^{\text{LoS}} = \frac{c}{4\pi f_m \bar{d}_l} e^{-\frac{1}{2} k_{\text{abs}}(f_m) \bar{d}_l} e^{-j \frac{2\pi f_m}{c} \bar{d}_l} \quad (5)$$

where c is the speed-of-light, $k_{\text{abs}}(f_m)$ is the SD molecular absorption coefficient for the m -th subcarrier frequency f_m and \bar{d}_l is the transmission distance [48, 50]. For NLoS paths, the expected path gain is given by

$$\mathbb{E}\{|\alpha_{l,m}^{\text{NLoS}}|^2\} = \left(\frac{c}{4\pi f_m \bar{d}_l}\right)^2 e^{-k_{\text{abs}}(f_m) \bar{d}_l} e^{-\frac{\bar{d}_l}{\bar{\Gamma}}}, \quad (6)$$

where $\bar{\tau}$ is the time of arrival of the l -th path while $\bar{\Gamma}$ denotes the ray decay factor [16]. We note here that the proposed hybrid beamforming techniques for THz channel are also applicable for both narrowband and wideband mmWave systems.

In (4), $\mathbf{a}'(\phi_l) \in \mathbb{C}^{N'}$ and $\mathbf{a}(\theta_l) \in \mathbb{C}^N$ are the steering vectors corresponding to the physical direction-of-arrival (DoA) (ϕ_l) and direction-of-departure (DoD) angles (θ_l) of the l -th paths, respectively. The n -th element of $\mathbf{a}(\theta_l)$ for a uniform linear array (ULA) is given by

$$[\mathbf{a}(\theta_l)]_n = \frac{1}{\sqrt{N}} \exp\{-j2\pi \frac{d}{\lambda_c} (n-1) \sin \theta_l\}, \quad (7)$$

where $n = 1, \dots, N$, λ_c is the wavelength of the central subcarrier frequency, i.e., $\lambda_c = \frac{c}{f_c}$, where f_c is the carrier frequency and d is the antenna element spacing, which is typically selected as $d = \lambda_c/2$. Note that the receive steering vector $\mathbf{a}'(\phi_l)$ can be defined similarly.

2) *Beam-Squint Effect*: In wideband transmission, it is typically assumed that a common analog beamformer is designed corresponding to a single wavelength for all subcarriers, i.e., $\lambda_1 = \dots = \lambda_M = \frac{c}{f_c}$. However, this assumption no longer holds when bandwidth is so large that the beams generated at different subcarriers squint and they point to different directions in spatial domain [4, 27, 28, 30]. If a similar beamforming architecture, employing SI analog beamformer and SD digital beamformers, is also utilized by the user, the same beam-squint effect is also observed at the user. The amount of beam-squint in the spatial domain is SD and it becomes larger as $|f_m - f_c|$ increases. Thus, we define the SD beam-squinted DoA and DoD angles in spatial domain as $\sin \varphi_{l,m}$ and $\sin \vartheta_{l,m}$, respectively. Then, the relationship

between the spatial and physical directions $(\sin \phi_l, \sin \theta_l)$ is given as

$$\sin \varphi_{l,m} = \eta_m \sin \phi_l, \quad \sin \vartheta_{l,m} = \eta_m \sin \theta_l, \quad (8)$$

where $\eta_m = \frac{f_m}{f_c}$, $f_m = f_c + \frac{B}{M}(m-1 - \frac{M-1}{2})$ is the m -th subcarrier frequency for the system bandwidth B . We can see beam-squint is mitigated if the spatial $(\sin \varphi_{l,m}, \sin \vartheta_{l,m})$ and physical directions $(\sin \phi_l, \sin \theta_l)$ are equal, i.e., $\eta_m = 1$.

Under the effect of beam-squint, the n -th entry of the SD steering vector $\mathbf{a}(\vartheta_{l,m})$ is given by

$$\begin{aligned} [\mathbf{a}(\vartheta_{l,m})]_n &= \frac{1}{\sqrt{N}} \exp \left\{ -j \frac{2\pi d}{\lambda_m} (n-1) \sin \theta_l \right\} \\ &= \frac{1}{\sqrt{N}} \exp \left\{ -j\pi \frac{f_m}{f_c} (n-1) \sin \theta_l \right\} \\ &= \frac{1}{\sqrt{N}} \exp \left\{ -j\pi (n-1) \eta_m \sin \theta_l \right\}, \end{aligned} \quad (9)$$

where $\lambda_m = \frac{c}{f_m}$ is the wavelength of the m -th subcarrier. Comparing (7) and (9) yields that the deviation in the spatial directions due to beam-squint can be compensated by exploiting the phase terms of the steering vectors as will be discussed in Sec. III-A2.

For communications-only problem, the hybrid beamforming design aims to maximize the SE which is defined for the m -th subcarrier as

$$\begin{aligned} \text{SE}[m] &= \log_2 \left| \mathbf{I}_{N'} + \frac{1}{N_{\text{ds}} \sigma^2} \mathbf{H}[m] \mathbf{F}_{\text{RF}} \mathbf{F}_{\text{BB}}[m] \right. \\ &\quad \left. \times \mathbf{F}_{\text{BB}}^{\text{H}}[m] \mathbf{F}_{\text{RF}}^{\text{H}} \mathbf{H}^{\text{H}}[m] \right|, \end{aligned} \quad (10)$$

for which the SE of the overall system is $\text{SE} = \sum_{m=1}^M \text{SE}[m]$. We note that maximizing the SE can be achieved by exploiting the similarity between the hybrid beamformer $\mathbf{F}_{\text{RF}} \mathbf{F}_{\text{BB}}[m]$ and the unconstrained communications-only beamformer $\mathbf{F}_{\text{C}}[m] \in \mathbb{C}^{K \times N_{\text{ds}}}$ [3, 17, 18]. In particular, $\mathbf{F}_{\text{C}}[m]$ is the subarray beamformer as

$$\mathbf{F}_{\text{C}}[m] = \mathbf{Q}^{\text{T}} \bar{\mathbf{F}}_{\text{C}}[m], \quad (11)$$

where $\bar{\mathbf{F}}_{\text{C}}[m] \in \mathbb{C}^{N \times N_{\text{ds}}}$ denotes the communications-only beamformer corresponding to the full array, and it can be directly obtained from the right singular matrix of $\bar{\mathbf{H}}[m]$ via singular value decomposition (SVD) [3].

Assumption 1: We assume that the THz channel matrix of the full array, i.e., $\bar{\mathbf{H}}[m]$ is available for ISAC beamformer design. This can be achieved either model-based techniques [32, 54, 55] or learning-based approaches [27, 56]. It is also worth noting that the complete channel matrix can be constructed by cycling the N_{RF} RF chains among N antennas during channel training. In other words, the RF chains are first connected to the first N_{RF} antennas during the first part of the training sequence, then the second N_{RF} antennas, and so on [3, 57].

B. Sensing Model

While communicating with the user, the ISAC system aims to deliver as high SNR as possible to targets for sensing [6, 58]. To that end, the BS transmits probing signals to sense the targets in the environment. Let $\tilde{\mathbf{X}}_t[m] \in \mathbb{C}^{N \times T_{\text{S}}}$ be the transmitted sensing signal, where T_{S} is the number of

snapshots. Then, the $K \times T_{\text{S}}$ received echo signal from T targets is

$$\tilde{\mathbf{Y}}[m] = \sum_{t=1}^T \beta_t \mathbf{a}(\Phi_t) \mathbf{a}^{\text{T}}(\Phi_t) \tilde{\mathbf{X}}[m] + \tilde{\mathbf{N}}[m], \quad (12)$$

where β_t represents the reflection coefficient, i.e., radar cross section, of the target, $\mathbf{a}(\Phi_t) \in \mathbb{C}^N$ denotes the steering vector corresponding to the t -th target at the direction Φ_t and $\tilde{\mathbf{N}}[m] \in \mathbb{C}^{N \times T_{\text{S}}}$ denotes the additive noise term. The estimation of the target directions can be performed via both model-based [58–60] and model-free learning-based [61] techniques available in the literature. Once the target directions are estimated as $\{\hat{\Phi}_t\}_{t \in \mathcal{T}}$, where $\mathcal{T} = \{1, \dots, T\}$, then the sensing-only beamformer $\bar{\mathbf{F}}_{\text{S}} \in \mathbb{C}^{N \times T}$ is constructed as

$$\bar{\mathbf{F}}_{\text{S}} = \left[\mathbf{a}(\hat{\Phi}_1), \dots, \mathbf{a}(\hat{\Phi}_T) \right]. \quad (13)$$

Then, the sensing-only subarray beamformer $\mathbf{F}_{\text{S}} \in \mathbb{C}^{K \times T}$ can be given by

$$\mathbf{F}_{\text{S}} = \mathbf{Q}^{\text{T}} \bar{\mathbf{F}}_{\text{S}}. \quad (14)$$

Assumption 2: We assume that the sensing-only full array beamformer $\bar{\mathbf{F}}_{\text{S}}$ is available. That is to say, the target directions are acquired during the search operation of the radar prior to the beamformer design. Although the relevant literature on the direction estimation is mostly limited to beam-squint-free scenario [59, 60, 62], a beam-squint-aware multiple signal classification (BSA-MUSIC) technique is introduced recently in [31] for the compensation of beam-squint in direction estimation problem.

C. Problem Formulation

Our aim in this work is to jointly optimize a subarray at the BS as well as designing hybrid beamformers, which can be achieved via maximizing the SE of the overall system. By exploiting the similarity between the hybrid beamformer $\mathbf{F}_{\text{RF}} \mathbf{F}_{\text{BB}}[m]$ and $\mathbf{F}_{\text{C}}[m]$, \mathbf{F}_{S} , the joint antenna selection and hybrid beamforming problem is written as

$$\begin{aligned} &\underset{\mathbf{Q}, \mathbf{F}_{\text{RF}}, \{\mathbf{F}_{\text{BB}}[m], \mathbf{D}[m]\}_{m \in \mathcal{M}}}{\text{minimize}} \sum_{m=1}^M \left(\varepsilon \|\mathbf{F}_{\text{RF}} \mathbf{F}_{\text{BB}}[m] - \mathbf{F}_{\text{C}}[m]\|_{\mathcal{F}} \right. \\ &\quad \left. + (1 - \varepsilon) \|\mathbf{F}_{\text{RF}} \mathbf{F}_{\text{BB}}[m] - \mathbf{F}_{\text{S}} \mathbf{D}[m]\|_{\mathcal{F}} \right) \end{aligned}$$

$$\text{subject to: } \sum_{m=1}^M \|\mathbf{F}_{\text{RF}} \mathbf{F}_{\text{BB}}[m]\|_{\mathcal{F}} = MN_{\text{ds}}, \quad (15a)$$

$$|[\mathbf{F}_{\text{RF}}]_{i,j}| = 1/\sqrt{N}, \quad (15b)$$

$$\mathbf{D}[m] \mathbf{D}^{\text{H}}[m] = \mathbf{I}_T, \quad (15c)$$

$$\mathbf{F}_{\text{C}}[m] = \mathbf{Q}^{\text{T}} \bar{\mathbf{F}}_{\text{C}}[m], \quad (15d)$$

$$\mathbf{F}_{\text{S}} = \mathbf{Q}^{\text{T}} \bar{\mathbf{F}}_{\text{S}}, \quad (15e)$$

$$[\mathbf{Q}]_{n,k} \in \{0, 1\}, \quad (15f)$$

$$\|\text{vec}\{\mathbf{Q}\}\|_0 = K, \quad (15g)$$

where $\mathbf{D}[m] \in \mathbb{C}^{T \times N_{\text{ds}}}$ is a unitary matrix (i.e., $\mathbf{D}[m] \mathbf{D}^{\text{H}}[m] = \mathbf{I}_T$) and it provides the change of dimensions

between \mathbf{F}_S and $\mathbf{F}_C[m]$. In (15), $0 \leq \varepsilon \leq 1$ is the trade-off parameter between communications and sensing tasks. Specifically, $\varepsilon = 1$ ($\varepsilon = 0$) corresponds to communications-only (sensing-only) design. The procedure of determining ε includes the ratio of allocated resources, such as power [63] and signal durations of the coherent processing intervals [64].

The problem in (15) falls to the class of mixed-integer non-convex programming (MINCP), which is difficult to solve due to several matrix variables $\mathbf{Q}, \mathbf{F}_{\text{RF}}, \mathbf{F}_{\text{BB}}[m], \mathbf{D}[m]$ and non-convex constraints. In particular, the constant-modulus constraints for the analog beamformers \mathbf{F}_{RF} in (15b) indicate that the amplitude of the analog beamformer weights are a constant. Furthermore, the antenna selection matrix \mathbf{Q} has binary values as in (15f) and, the number of non-zero terms in \mathbf{Q} equals to K as in (15g). Following these considerations, we introduce an effective and computationally-efficient solution in the remainder of this work.

III. JOINT ANTENNA SELECTION AND BEAMFORMER DESIGN

In order to provide an effective solution, we first divide the problem in (15) into two subproblems, hybrid beamforming and antenna selection. In hybrid beamforming design, we first formulate the subproblem as a manifold optimization problem for a given subarray configuration, wherein the hybrid analog/digital beamformers are alternately optimized as well as the impact of beam-squint is compensated.

In antenna selection, we are interested in selecting K out of N antenna elements at the BS. This yields $P = \binom{N}{K} = \frac{N!}{K!(N-K)!}$ possible subarray configurations. Therefore, antenna selection problem can be viewed as a classification problem with P classes. Define $\mathcal{Q} = \{\mathbf{Q}_1, \dots, \mathbf{Q}_P\}$ as the set of all possible subarray configurations, where \mathbf{Q}_p represents the selection matrix \mathbf{Q} for the p -th configuration as $\mathbf{Q}_p = [\mathbf{q}_1^p, \dots, \mathbf{q}_K^p]$. Here, $\mathbf{q}_k^p = [0, \dots, q_{n,k}^p, \dots, 0]^T$, and we have $q_{n,k}^p = 1$ corresponding to the k -th element of the subarray as the selected n -th transmit antenna for the p -th configuration.

A. Hybrid Beamformer Design

We first define the hybrid beamformers for the p -th subarray configuration as $\mathbf{F}_{\text{RF}}^{(p)} \in \mathbb{C}^{K \times N_{\text{RF}}}$ and $\mathbf{F}_{\text{BB}}^{(p)}[m] \in \mathbb{C}^{N_{\text{RF}} \times N_{\text{ds}}}$. Next, we define the cost function in (15) for the p -th configuration and the m -th subcarrier as

$$f(p, m) = \varepsilon \|\mathbf{F}_{\text{RF}}^{(p)} \mathbf{F}_{\text{BB}}^{(p)}[m] - \mathbf{F}_C^{(p)}[m]\|_{\mathcal{F}} + (1 - \varepsilon) \|\mathbf{F}_{\text{RF}}^{(p)} \mathbf{F}_{\text{BB}}^{(p)}[m] - \mathbf{F}_S^{(p)} \mathbf{D}^{(p)}[m]\|_{\mathcal{F}}, \quad (16)$$

where $\mathbf{F}_C^{(p)}[m] = \mathbf{Q}_p \bar{\mathbf{F}}_C[m]$ and $\mathbf{F}_S^{(p)} = \mathbf{Q}_p \bar{\mathbf{F}}_S$. Using triangle inequality, the following can be obtained, i.e.,

$$\begin{aligned} f(p, m) &\geq \|\varepsilon \mathbf{F}_{\text{RF}}^{(p)} \mathbf{F}_{\text{BB}}^{(p)}[m] - \varepsilon \mathbf{F}_C^{(p)}[m]\|_{\mathcal{F}} \\ &+ (1 - \varepsilon) \|\mathbf{F}_{\text{RF}}^{(p)} \mathbf{F}_{\text{BB}}^{(p)}[m] - (1 - \varepsilon) \mathbf{F}_S^{(p)} \mathbf{D}^{(p)}[m]\|_{\mathcal{F}} \\ &= \|\mathbf{F}_{\text{RF}}^{(p)} \mathbf{F}_{\text{BB}}^{(p)}[m] - \underbrace{\varepsilon \mathbf{F}_C^{(p)}[m] - (1 - \varepsilon) \mathbf{F}_S^{(p)} \mathbf{D}^{(p)}[m]}_{\triangleq \mathbf{F}_{\text{SC}}^{(p)}[m]}\|_{\mathcal{F}}, \end{aligned} \quad (17)$$

where we define $\mathbf{F}_{\text{SC}}^{(p)}[m] \in \mathbb{C}^{K \times N_{\text{ds}}}$ as the joint sensing-communications (JSC) beamformer, which involves the combination of $\mathbf{F}_C^{(p)}[m]$ and $\mathbf{F}_S^{(p)}$ [5, 6, 47] as

$$\mathbf{F}_{\text{SC}}^{(p)}[m] = \varepsilon \mathbf{F}_C^{(p)}[m] + (1 - \varepsilon) \mathbf{F}_S^{(p)} \mathbf{D}^{(p)}[m]. \quad (18)$$

Since we have $f(p, m) \geq \|\mathbf{F}_{\text{RF}}^{(p)} \mathbf{F}_{\text{BB}}^{(p)}[m] - \mathbf{F}_{\text{SC}}^{(p)}[m]\|_{\mathcal{F}}$ from (17), maximizing $\|\mathbf{F}_{\text{RF}}^{(p)} \mathbf{F}_{\text{BB}}^{(p)}[m] - \mathbf{F}_{\text{SC}}^{(p)}[m]\|_{\mathcal{F}}$ is equivalent to maximizing $f(p, m)$. Thus, we can write the hybrid beamforming design problem for the p -th subarray configuration as

$$\begin{aligned} &\underset{\mathbf{F}_{\text{RF}}^{(p)}, \mathbf{F}_{\text{BB}}^{(p)}[m], \mathbf{D}^{(p)}[m]}{\text{minimize}} && \sum_{m=1}^M \|\mathbf{F}_{\text{RF}}^{(p)} \mathbf{F}_{\text{BB}}^{(p)}[m] - \mathbf{F}_{\text{SC}}^{(p)}[m]\|_{\mathcal{F}} \\ &\text{subject to:} && \|\mathbf{F}_{\text{RF}}^{(p)}\|_{k,n} = 1/\sqrt{K}, \\ &&& \sum_{m=1}^M \|\mathbf{F}_{\text{RF}}^{(p)} \mathbf{F}_{\text{BB}}^{(p)}[m]\|_{\mathcal{F}} = MN_{\text{ds}}, \\ &&& \mathbf{D}^{(p)}[m] \mathbf{D}^{(p)H}[m] = \mathbf{I}_T, \end{aligned} \quad (19)$$

which can be written in a compact form as

$$\begin{aligned} &\underset{\mathbf{F}_{\text{RF}}^{(p)}, \tilde{\mathbf{F}}_{\text{BB}}^{(p)}, \tilde{\mathbf{D}}^{(p)}}{\text{minimize}} && \|\mathbf{F}_{\text{RF}}^{(p)} \tilde{\mathbf{F}}_{\text{BB}}^{(p)} - \tilde{\mathbf{F}}_{\text{SC}}^{(p)}\|_{\mathcal{F}} \\ &\text{subject to:} && \|\mathbf{F}_{\text{RF}}^{(p)}\|_{k,n} = 1/\sqrt{K}, \\ &&& \|\mathbf{F}_{\text{RF}}^{(p)} \tilde{\mathbf{F}}_{\text{BB}}^{(p)}\|_{\mathcal{F}} = MN_{\text{ds}}, \\ &&& \tilde{\mathbf{D}}^{(p)} \tilde{\mathbf{D}}^{(p)H} = \mathbf{I}_T, \end{aligned} \quad (20)$$

where $\tilde{\mathbf{F}}_{\text{BB}}^{(p)} = [\mathbf{F}_{\text{BB}}^{(p)}[1], \dots, \mathbf{F}_{\text{BB}}^{(p)}[M]]$, $\tilde{\mathbf{F}}_{\text{SC}}^{(p)} = [\mathbf{F}_{\text{SC}}^{(p)}[1], \dots, \mathbf{F}_{\text{SC}}^{(p)}[M]]$ and $\tilde{\mathbf{D}}^{(p)} = [\mathbf{D}^{(p)}[1], \dots, \mathbf{D}^{(p)}[M]]$ are $K \times MN_{\text{ds}}$, $K \times MN_{\text{ds}}$ and $T \times MN_{\text{ds}}$ matrices, respectively.

Now, the optimization problem in (20) can be solved effectively via manifold optimization techniques [18, 65, 66]. To solve (20), we follow an alternating technique, wherein the unknown variables $\mathbf{F}_{\text{RF}}^{(p)}$, $\tilde{\mathbf{F}}_{\text{BB}}^{(p)}$ and $\tilde{\mathbf{D}}^{(p)}$ are estimated one by one while the remaining terms are fixed.

1) *Solve for $\mathbf{F}_{\text{RF}}^{(p)}$* : In order to solve for $\mathbf{F}_{\text{RF}}^{(p)}$ via manifold optimization, we first define $\mathbf{f}^{(p)} = \text{vec}\{\mathbf{F}_{\text{RF}}^{(p)}\} \in \mathbb{C}^{KN_{\text{RF}}}$ as the vectorized form of $\mathbf{F}_{\text{RF}}^{(p)}$. By exploiting the unit-modulus constraint of the analog beamformer, the search space for $\mathbf{f}^{(p)}$ is regarded as *Riemannian submanifold* \mathcal{R} of the complex plane $\mathbb{C}^{KN_{\text{RF}}}$ as [65, 67]

$$\mathcal{R} = \{\mathbf{f}^{(p)} \in \mathbb{C}^{KN_{\text{RF}}} : \|\mathbf{f}^{(p)}\|_1 = \dots = \|\mathbf{f}^{(p)}\|_{KN_{\text{RF}}} = \frac{1}{\sqrt{K}}\}. \quad (21)$$

Then, by following a conjugate gradient descent technique [66, 68], $\mathbf{f}^{(p)}$ can be optimized iteratively, and in the i -th iteration, we have

$$\mathbf{f}_i^{(p)} = \frac{\mathbf{f}_i^{(p)} + \dot{a}_i \boldsymbol{\xi}_i(\mathbf{f}_i, \tilde{\mathbf{F}}_{\text{BB}}^{(p)}, \tilde{\mathbf{F}}_{\text{SC}}^{(p)})}{\|\mathbf{f}_i^{(p)} - \dot{a}_i \boldsymbol{\xi}_i\|}, \quad (22)$$

where \dot{a}_i is Armijo backtracking line search step size [69] and $\boldsymbol{\xi}_i(\mathbf{f}_i, \tilde{\mathbf{F}}_{\text{BB}}^{(p)}, \tilde{\mathbf{F}}_{\text{SC}}^{(p)}) \in \mathbb{C}^{KN_{\text{RF}}}$ is the directional gradient vector [65], and it depends on the Riemannian gradient of $\mathbf{f}_i^{(p)}$,

i.e., $\nabla_{\mathcal{R}} \mathbf{f}_i^{(p)}$, which is defined as

$$\nabla_{\mathcal{R}} \mathbf{f}_i^{(p)} = \nabla \mathbf{f}_i^{(p)} - \text{Re}\{\nabla \mathbf{f}_i^{(p)} \odot \mathbf{f}_i^{(p)*}\} \odot \mathbf{f}_i^{(p)}, \quad (23)$$

where $\nabla \mathbf{f}_i^{(p)}$ denotes the Euclidean gradient of \mathbf{f}_i as

$$\nabla \mathbf{f}_i^{(p)} = -2\mathbf{B}^{(p)} \left(\mathbf{f}_{\text{SC}}^{(p)} - \mathbf{B}^{(p)} \mathbf{f}_i^{(p)} \right), \quad (24)$$

where $\mathbf{B}^{(p)} = \tilde{\mathbf{F}}_{\text{BB}}^{(p)\top} \otimes \mathbf{I}_K \in \mathbb{C}^{KM N_{\text{ds}} \times KN_{\text{RF}}}$ and $\mathbf{f}_{\text{SC}}^{(p)} = \text{vec}\{\tilde{\mathbf{F}}_{\text{SC}}^{(p)}\} \in \mathbb{C}^{KM N_{\text{ds}}}$.

Given $\tilde{\mathbf{F}}_{\text{BB}}^{(p)}$ and $\tilde{\mathbf{F}}_{\text{SC}}^{(p)}$, the optimization process can be initialized for $i = 0$ by selecting $\mathbf{f}_0^{(p)}$ as $[\mathbf{f}_0^{(p)}]_k = e^{j\Psi_k}$, where $\Psi_k \sim \text{uniform}([0, 2\pi])$ for $k = 1, \dots, KN_{\text{RF}}$. The complexity of computing (22) is mainly due to the computation of the conjugate gradient in (24). Therefore, the computational complexity order of optimizing $\mathbf{F}_{\text{RF}}^{(p)}$ is $O(N_{\text{iter}}^A K^2 N_{\text{RF}} M N_{\text{ds}})$, where N_{iter}^A is the number of iterations [6, 68].

2) Solve for $\tilde{\mathbf{F}}_{\text{BB}}^{(p)}$ and Beam-Squint Compensation (BSC):

Since the analog beamformer $\mathbf{F}_{\text{RF}}^{(p)}$ is SI, beam-squint occurs. In order to compensate for the impact of beam-squint, we design the baseband beamformer $\mathbf{F}_{\text{BB}}^{(p)}[m]$ accordingly such that the impact of beam-squint in the analog domain is conveyed to the baseband which is SD. To this end, we first obtain $\mathbf{F}_{\text{BB}}^{(p)}[m]$ from $\mathbf{F}_{\text{SC}}^{(p)}[m]$ and $\mathbf{F}_{\text{RF}}^{(p)}$. Then, update the baseband beamformer by utilizing SD analog beamformer, which can be virtually computed from the SI analog beamformer $\mathbf{F}_{\text{RF}}^{(p)}$ [31].

Given $\mathbf{F}_{\text{BB}}^{(p)}[m]$ from $\tilde{\mathbf{F}}_{\text{SC}}^{(p)}$ and $\mathbf{F}_{\text{RF}}^{(p)}$, a straightforward solution for $\mathbf{F}_{\text{BB}}^{(p)}[m]$ is

$$\check{\mathbf{F}}_{\text{BB}}^{(p)}[m] = \left(\mathbf{F}_{\text{RF}}^{(p)} \right)^\dagger \mathbf{F}_{\text{SC}}^{(p)}[m]. \quad (25)$$

Now, we define the SD analog beamformer as $\check{\mathbf{F}}_{\text{RF}}^{(p)}[m] \in \mathbb{C}^{K \times N_{\text{RF}}}$, which can be found from $\mathbf{F}_{\text{RF}}^{(p)}$ as

$$\check{\mathbf{F}}_{\text{RF}}^{(p)}[m] = \frac{1}{\sqrt{K}} \boldsymbol{\Omega}_m^{(p)}, \quad (26)$$

where $\boldsymbol{\Omega}_m^{(p)} \in \mathbb{C}^{K \times N_{\text{RF}}}$ includes the phase information of the SI beamformer $\mathbf{F}_{\text{RF}}^{(p)}$ as

$$[\boldsymbol{\Omega}_m^{(p)}]_{k,n} = \exp\{j\eta_m \angle \{[\mathbf{F}_{\text{RF}}^{(p)}]_{k,n}\}\}, \quad (27)$$

for $k = 1, \dots, K$ and $n = 1, \dots, N_{\text{RF}}$. Notice that the SD beamformer in (26) and (27) includes the compensation of beam-squint via multiplying the phase terms by η_m . Next, we update the baseband beamformer in (25) such that our hybrid beamformer $\mathbf{F}_{\text{RF}}^{(p)} \mathbf{F}_{\text{BB}}^{(p)}[m]$ resembles the SD JSC beamformer $\mathbf{F}_{\text{SC}}^{(p)}[m]$ as much as possible. Hence, from (25), the updated baseband beamformer is computed as

$$\mathbf{F}_{\text{BB}}^{(p)}[m] = \left(\mathbf{F}_{\text{RF}}^{(p)} \right)^\dagger \check{\mathbf{F}}_{\text{RF}}^{(p)}[m] \check{\mathbf{F}}_{\text{BB}}^{(p)}[m]. \quad (28)$$

3) Solve for $\tilde{\mathbf{D}}^{(p)}$: Given $\mathbf{F}_{\text{RF}}^{(p)}$, $\tilde{\mathbf{F}}_{\text{BB}}^{(p)}$ and $\tilde{\mathbf{F}}_{\text{SC}}^{(p)}$, the auxiliary variable $\tilde{\mathbf{D}}^{(p)}$ can be optimized via

$$\begin{aligned} & \underset{\tilde{\mathbf{D}}^{(p)}}{\text{minimize}} \quad \|\mathbf{F}_{\text{RF}}^{(p)} \tilde{\mathbf{F}}_{\text{BB}}^{(p)} - \tilde{\mathbf{F}}_{\text{SC}}^{(p)}\|_{\mathcal{F}} \\ & \text{subject to:} \quad \tilde{\mathbf{D}}^{(p)} \tilde{\mathbf{D}}^{(p)\text{H}} = \mathbf{I}_T, \end{aligned} \quad (29)$$

which is called orthogonal Procrustes problem [31], and its

Algorithm 1 ISAC Hybrid Beamforming With BSC

Input: Subarray index p , $\bar{\mathbf{F}}_S$, $\bar{\mathbf{H}}[m]$, η_m and ε .

- 1: Compute $\bar{\mathbf{F}}_C[m]$ from $\bar{\mathbf{H}}[m]$.
- 2: Construct \mathbf{Q}_p .
- 3: Initialize $\mathbf{F}_C^{(p)}[m] = \mathbf{Q}_p \bar{\mathbf{F}}_C[m]$, $\mathbf{F}_S^{(p)} = \mathbf{Q}_p \bar{\mathbf{F}}_S$, $\mathbf{F}_{\text{RF}}^{(p,j)}$ and $\tilde{\mathbf{D}}^{(p,j)} = \mathbf{I}_{T \times M N_{\text{ds}}}$ for $j = 1$.
- 4: **while** $\delta_j < \bar{\delta}$ **do**
- 5: $\mathbf{F}_{\text{SC}}^{(p,j)}[m] \leftarrow \varepsilon \mathbf{F}_C^{(p)}[m] + (1 - \varepsilon) \mathbf{F}_S^{(p)} \mathbf{D}^{(p,j)}[m]$.
- 6: $\mathbf{f}_{j,i}^{(p)} \leftarrow \text{vec}\{\mathbf{F}_{\text{RF}}^{(p,j)}\}$.
- 7: **while**
- 8: Choose Armijo backtracking step size \hat{a}_i .
- 9: Compute the gradient $\nabla_{\mathcal{R}} \mathbf{f}_{j,i}^{(p)}$ in (23).
- 10: Update $\mathbf{f}_{j,i}^{(p)}$ from (22).
- 11: $i \leftarrow i + 1$.
- 12: **until** convergence
- 13: $\mathbf{F}_{\text{RF}}^{(p,j)} \leftarrow \text{vec}^{-1}\{\mathbf{f}_{j,i}^{(p)}\}$.
- 14: Compute $\check{\mathbf{F}}_{\text{RF}}^{(p)}[m]$ from (26) and (27).
- 15: Compute $\check{\mathbf{F}}_{\text{BB}}^{(p)}[m]$ from (25).
- 16: Using $\check{\mathbf{F}}_{\text{RF}}^{(p)}[m]$ and $\check{\mathbf{F}}_{\text{BB}}^{(p)}[m]$, update $\mathbf{F}_{\text{BB}}^{(p)}[m]$ as in (28) for beam-squint compensation.
- 17: Update $\mathbf{D}^{(p)}[m]$ as in (30).
- 18: $\delta_j = \|\mathbf{F}_{\text{RF}}^{(p)} \tilde{\mathbf{F}}_{\text{BB}}^{(p)} - \tilde{\mathbf{F}}_{\text{SC}}^{(p)}\|_{\mathcal{F}}$
- 19: $j \leftarrow j + 1$.
- 20: **end**

Return: Hybrid beamformers $\mathbf{F}_{\text{RF}}^{(p)}$ and $\mathbf{F}_{\text{BB}}^{(p)}[m]$.

solution is

$$\tilde{\mathbf{D}}^{(p)} = \mathbf{U} \mathbf{I}_{T \times M N_{\text{ds}}} \mathbf{V}, \quad (30)$$

where $\mathbf{U} \boldsymbol{\Sigma} \mathbf{V} = \mathbf{F}_S^{(p)\text{H}} \mathbf{F}_{\text{RF}} \tilde{\mathbf{F}}_{\text{BB}}^{(p)}$ is the SVD of the $T \times M N_{\text{ds}}$ matrix $\frac{1}{1-\varepsilon} \mathbf{F}_S^{(p)\text{H}} \left(\mathbf{F}_{\text{RF}}^{(p)} \tilde{\mathbf{F}}_{\text{BB}}^{(p)} - \tilde{\mathbf{F}}_{\text{SC}}^{(p)} \right)$, and $\mathbf{I}_{T \times M N_{\text{ds}}} = [\mathbf{I}_T | \mathbf{0}_{M N_{\text{ds}} - T \times T}^\top]$.

In Algorithm 1, the algorithmic steps of the proposed subarrayed beamforming approach are presented. Specifically, for a given subarray configuration index p , we first construct the subarray terms $\mathbf{F}_C^{(p)}[m]$ and $\mathbf{F}_S^{(p)}$ from the full array quantities. Then, for the first iteration, i.e., $j = 1$, the unknown variables are initialized as $\tilde{\mathbf{D}}^{(p,j)} = \mathbf{I}_{T \times M N_{\text{ds}}}$ and $\mathbf{F}_{\text{RF}}^{(p,j)} = e^{j\Psi}$, where $[\Psi]_{k,n} \sim \text{uniform}([0, 2\pi])$ for $k = 1, \dots, K$ and $n = 1, \dots, N_{\text{RF}}$. During alternating optimization, firstly, the analog beamformer $\mathbf{F}_{\text{RF}}^{(p)}$ is optimized in the steps 7-12. Then, the virtual SD analog beamformer $\check{\mathbf{F}}_{\text{RF}}^{(p)}[m]$ is computed, and the baseband beamformer is updated for BSC in steps 15-16. Finally, the auxiliary variable $\mathbf{D}^{(p)}[m]$ is updated in step 17. The hybrid beamformers are obtained when the algorithm converges [6, 66, 68].

B. Antenna Selection

Given the hybrid beamformers $\mathbf{F}_{\text{RF}}^{(p)}$, $\mathbf{F}_{\text{BB}}^{(p)}[m]$, we can write the SE when the p -th subarray is selected as

$$\begin{aligned} \text{SE}_p[m] &= \log_2 |\mathbf{I}_{N'} + \frac{1}{N_{\text{ds}} \sigma^2} \mathbf{H}^{(p)}[m] \mathbf{F}_{\text{RF}}^{(p)} \mathbf{F}_{\text{BB}}^{(p)}[m] \\ &\quad \times \mathbf{F}_{\text{RF}}^{(p)} \mathbf{F}_{\text{BB}}^{(p)\text{H}}[m] \mathbf{H}^{(p)\text{H}}[m]|, \end{aligned} \quad (31)$$

and the SE over all subcarriers is $\text{SE}_p = \sum_{m=1}^M \text{SE}_p[m]$. Using (31), the antenna selection problem is written as

$$\begin{aligned} p^* &= \arg \max_p \text{SE}_p \\ \text{subject to: } \mathbf{H}^{(p)}[m] &= \overline{\mathbf{H}}[m] \mathbf{Q}_p, \end{aligned} \quad (32)$$

where p^* represents the best subarray configuration maximizing the SE.

Now, we discuss the optimality of the best subarray configuration under the impact of beam-squint. Define $\mathbf{u}_{p^*}(\theta) = \mathbf{Q}_{p^*}^T \mathbf{a}(\theta)$ as the $K \times 1$ beam-squint-free best subarray steering vector corresponding to an arbitrary direction θ . Then, it is clear that $\mathbf{u}_{p^*}(\theta)$ achieves the highest SE in (32) and obtains the maximum array gain $A_G(\Phi)$ for an arbitrary direction Φ if $\Phi = \theta$, i.e., $\theta = \arg \text{maximize}_{\Phi} A_G(\Phi)$, where

$$A_G(\Phi) = |\mathbf{u}_{p^*}^H(\theta) \mathbf{u}_{p^*}(\Phi)|^2 / N^2. \quad (33)$$

In the following theorem, we show that the array gain, and equivalently the SE [31, 70, 71], is maximized only if two conditions are met, i.e., the best subarray configuration is selected and beam-squint is completely compensated.

Theorem 1. Define $\mathbf{u}_p(\vartheta_m) = \mathbf{Q}_p^T \mathbf{a}(\vartheta_m)$ as the $K \times 1$ beam-squint-corrupted subarray steering vector corresponding to an arbitrary direction θ and subcarrier $m \in \mathcal{M}$ as defined in (9). Then, $\mathbf{u}_p(\vartheta_m)$ achieves the maximum array gain only if

$$\sin \vartheta_m = \eta_m \sin \theta, \quad p = p^*, \quad (34)$$

where p^* is the optimizer of (32), and the array gain varying across the whole bandwidth is

$$A_G(\vartheta_m) = \frac{|\mathbf{u}_{p^*}^H(\theta) \mathbf{u}_{p^*}(\vartheta_m)|^2}{N^2}. \quad (35)$$

Proof: We first prove the condition $p = p^*$ is required for the maximization of array gain in (35). Thus, we start by rewriting the array gain across the subcarriers in (35) as

$$\begin{aligned} A_G(\vartheta_m) &= \frac{|\mathbf{u}_{p^*}^H(\theta) \mathbf{u}_{p^*}(\vartheta_m)|^2}{N^2} \\ &= \frac{|\mathbf{a}^H(\theta) \mathbf{Q}_{p^*} \mathbf{Q}_{p^*}^T \mathbf{a}(\vartheta_m)|^2}{N^2} \\ &= \frac{\text{Trace}\{\mathbf{Q}_{p^*} \mathbf{Q}_{p^*}^T\} |\mathbf{a}^H(\theta) \mathbf{a}(\vartheta_m)|^2}{N^2}, \end{aligned} \quad (36)$$

where the first term in the nominator, i.e., $\text{Trace}\{\mathbf{Q}_{p^*} \mathbf{Q}_{p^*}^T\}$, is maximized as $\max_p \text{Trace}\{\mathbf{Q}_p \mathbf{Q}_p^T\} = K$, which can be achieved only if $p = p^*$ when $\mathbf{Q}_{p^*} \mathbf{Q}_{p^*}^T = \mathbf{I}_K$.

Now, we show that maximum array gain is only achieved when $\sin \vartheta_{l,m} = \eta_m \sin \theta_l$. Thus, substituting $\mathbf{Q}_{p^*} \mathbf{Q}_{p^*}^T = \mathbf{I}_K$

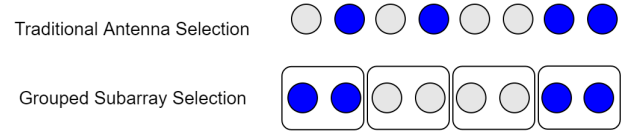


Fig. 3. An example of selecting 4 out of 8 antennas for traditional antenna selection and GSS, wherein the antennas are picked individually and in groups of size G , respectively.

in (36) yields

$$\begin{aligned} A_G(\vartheta_m) &= \frac{|\mathbf{a}^H(\theta) \mathbf{a}(\vartheta_m)|^2}{N^2} \\ &= \frac{1}{N^2} \left| \sum_{n_1=1}^N \sum_{n_2=1}^N e^{-j\pi((n_1-1) \sin \vartheta_m - (n_2-1) \frac{\lambda_c \sin \theta}{\lambda_m})} \right|^2 \\ &= \left| \sum_{n=0}^{N-1} \frac{e^{-j2\pi n \bar{d} (\frac{\sin \vartheta_m}{\lambda_c} - \frac{\sin \theta}{\lambda_m})}}{N} \right|^2 \\ &= \left| \sum_{n=0}^{N-1} \frac{e^{-j2\pi n \bar{d} (f_c \sin \vartheta_m - f_m \sin \theta)}}{N} \right|^2 \\ &= \left| \frac{1 - e^{-j2\pi N \bar{d} (f_c \sin \vartheta_m - f_m \sin \theta)}}{N(1 - e^{-j2\pi \bar{d} (f_c \sin \vartheta_m - f_m \sin \theta)})} \right|^2 \\ &= \left| \frac{\sin(\pi N \mu_m)}{N \sin(\pi \mu_m)} \right|^2 = |\zeta(\mu_m)|^2, \end{aligned} \quad (37)$$

where $\mu_m = \bar{d} (f_c \sin \vartheta_m - f_m \sin \theta)$. Due to the power focusing capability of the Dirichlet sinc function $\zeta(\mu_m)$ in (37), array gain is focused only on a small portion of the beamspace, and it substantially reduces across the subcarriers as $|f_m - f_c|$ increases. Furthermore, $|\zeta(\mu_m)|^2$ gives peak when $\mu_m = 0$, i.e., $f_c \sin \vartheta_m - f_m \sin \theta = 0$, which yields $\sin \vartheta_m = \eta_m \sin \theta$. ■

The problem in (32) requires to visit all possible subarray configurations, which can be computationally prohibitive and consume too much memory resources, especially when N is large, e.g., $N \geq 32$. To reduce this cost, we propose low complexity algorithms in the following.

1) *Grouped Subarray Selection:* In order to reduce the computational cost involved in the solution of (32), we propose GSS strategy to lower the number of possible subarray configurations. In GSS, the whole array is divided into $N_G = \frac{N}{G}$ disjoint groups, each of which includes G consecutive antennas as illustrated in Fig. 3. Thus, the antenna selection problem with GSS reduces to selecting $K_G = \frac{K}{G}$ groups out of N_G , and the number of possible subarray configurations with GSS is $P_G = \frac{N_G!}{K_G!(N_G - K_G)!}$. Then, the set of all possible subarray configurations with GSS is $\mathcal{Q}_G = \{\mathbf{Q}_1, \dots, \mathbf{Q}_{P_G}\}$, where \mathbf{Q}_{p_G} represents the antenna selection matrix for the p_G -th configuration, $p_G = 1, \dots, P_G$.

The grouped array structure significantly reduces the number of subarray configurations, even for small number of grouped antennas, e.g., $G = 2$. As an example, consider the scenario when $N = 64$ and $K = 32$. Then, the number of subarray configurations is $P = 1.83 \times 10^{18}$, which reduces to approximately $P_2 = 6 \times 10^9$ (3×10^9 times fewer) and

Algorithm 2 ISAC Beamforming & Antenna Selection

Input: $N, K, \bar{\mathbf{F}}_S, \bar{\mathbf{H}}[m], \forall m, P, B$.

- 1: Initialize $\text{SE}_0 = 0$,
- 2: **for** $b = 1, \dots, B$ **do**
- 3: Construct \mathcal{Q}^b .
- 4: **for** $p \in \{\frac{P(b-1)}{B} + 1, \dots, \frac{Pb}{B}\}$ **do**
- 5: Construct \mathbf{Q}_p .
- 6: $\mathbf{H}^{(p)}[m] = \bar{\mathbf{H}}[m] \mathbf{Q}_p, \forall m$.
- 7: Compute $\mathbf{F}_{\text{RF}}^{(p)}$ and $\mathbf{F}_{\text{BB}}^{(p)}[m]$ from Algorithm 1.
- 8: Compute SE_p from (31).
- 9: **end**
- 10: Solve for q_b^* as $q_b^* = \arg \max_{q_b} \text{SE}_{q_b}$.
- 11: $q_b^* \leftarrow \begin{cases} q_b^*, & \text{if } \text{SE}_{q_{b-1}^*} < \text{SE}_{q_b^*}, \\ q_{b-1}^*, & \text{otherwise} \end{cases}$.
- 12: Save q_b^* and clear the memory of $\mathbf{F}_{\text{RF}}^{(p)}, \mathbf{F}_{\text{BB}}^{(p)}[m]$ and $\mathbf{H}^{(p)}[m], \forall m, p$.
- 13: **end for**
- 14: **Return** Best subarray configuration index $q^* = q_B^*$, and the hybrid beamformers $\mathbf{F}_{\text{RF}}^{(q^*)}$ and $\mathbf{F}_{\text{BB}}^{(q^*)}[m]$.

$P_4 = 12870$ (1.4×10^{14} times fewer) for $G = 2$ and $G = 4$, respectively.

2) *Sequential Search Algorithm:* During the computation of SE_p for very large number of P , the computation platform requires very large amount of memory to save the variables whose dimensions are proportional to P . To efficiently use the memory, we devise a sequential search algorithm, wherein \mathcal{Q} is partitioned into B disjoint blocks as $\mathcal{Q} = \cup_{b=1}^B \mathcal{Q}^b$, where $\mathcal{Q}^b = \{\mathcal{Q}_{\frac{P(b-1)}{B}+1}, \dots, \mathcal{Q}_{\frac{Pb}{B}}\}$. Then, (32) is sequentially solved such that the variables, e.g., $\mathbf{F}_{\text{RF}}^{(p)}, \mathbf{F}_{\text{BB}}^{(p)}[m]$ and $\mathbf{H}^{(p)}[m]$ for $p \in \{\frac{P(b-1)}{B} + 1, \dots, \frac{Pb}{B}\}$, are removed from the memory after computation at the block b , instead of storing all the data in the memory. As a result, the computational platform requires approximately B times less memory.

In Algorithm 2, we present the algorithmic steps of the proposed approach for ISAC hybrid beamformer design with antenna selection. First, we compute \mathcal{Q}^b , i.e., the set of subarray configurations for the b -th block. Then, we design the hybrid beamformers and the cost (i.e., SE) is computed. Next, the computed costs of two consecutive blocks (i.e., $\text{SE}_{q_{b-1}^*}$ and $\text{SE}_{q_b^*}$) are compared, and the unnecessary variables are removed from the memory. Following this strategy, $\forall b$, the best subarray index q^* and the hybrid beamformers $\mathbf{F}_{\text{RF}}^{(q^*)}$ and $\mathbf{F}_{\text{BB}}^{(q^*)}[m]$.

C. Learning-Based Antenna Selection

Due to the combinatorial nature of antenna selection problem, it is preferable to formulate the problem as a classification problem, wherein each subarray configuration is regarded as a class. Thus, we design a classification model with a CNN architecture as shown in Fig. 4. Define $\mathcal{D} = \{\mathcal{D}_1, \dots, \mathcal{D}_1\}$ as the training dataset, where $\mathcal{D}_i = (\mathcal{I}_i, \mathcal{O}_i)$ denotes the i -th input and output data for $i = 1, \dots, I$. The input of the CNN is formed from the combination of communications

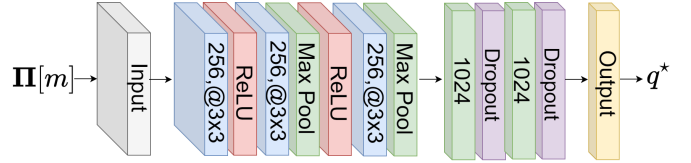


Fig. 4. The CNN architecture for antenna selection.

(channel matrix) and sensing (received target responses) data $\mathbf{\Pi}[m] \in \mathbb{C}^{N \times (N'+T)}$ as

$$\mathbf{\Pi}[m] = \begin{bmatrix} \underbrace{\bar{\mathbf{H}}^T[m]}_{\text{Communications}} & \underbrace{\bar{\mathbf{F}}_S}_{\text{Sensing}} \end{bmatrix}^T. \quad (38)$$

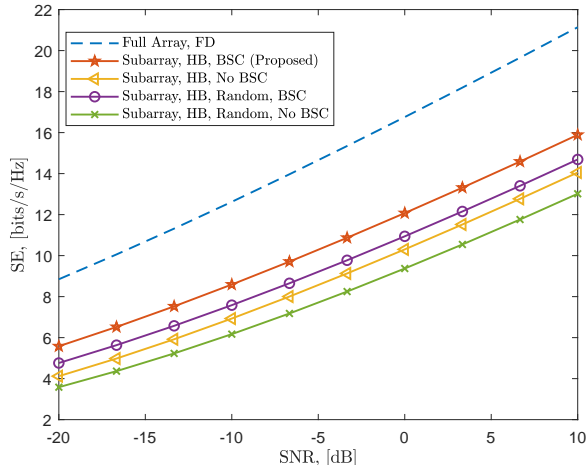
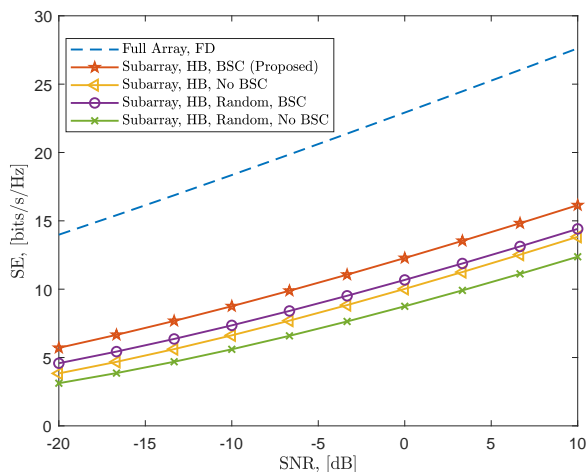
Define $\mathbf{\Pi}^{(i)}[m] \in \mathbb{C}^{N \times (N'+T)}$ as the generated data for the i -th sample of the dataset. Then, the input includes the real and imaginary parts of $\mathbf{\Pi}^{(i)}[m]$ as $\mathcal{X}_{i,1} = \text{Re}\{\mathbf{\Pi}^{(i)}[m]\}$ and $\mathcal{X}_{i,2} = \text{Im}\{\mathbf{\Pi}^{(i)}[m]\}$, respectively. Thus, \mathcal{X}_i is a “two-channel” real-valued tensor variable with the size of $N \times (N'+T) \times 2$. Furthermore, the output of the i -th sample is represented the best subarray index obtained from Algorithm 2 as $\mathcal{O}_i = q_{(i)}^*$. As a result, the output includes possible subarray configurations as $\mathcal{O}_i \in \mathcal{Q}$. Let $\boldsymbol{\theta} \in \mathbb{R}^U$ denote the learnable parameters of the CNN. Then, the learning model aims to construct the non-linear mapping between the input \mathcal{I}_i and the output label \mathcal{O}_i as $\mathcal{F}(\boldsymbol{\theta}, \mathcal{I}_i) \rightarrow \mathcal{O}_i$.

The CNN architecture for antenna selection has 13 layers as shown in Fig. 4. The first layer is the input layer with the size of $N \times (N'+T) \times 2$. The {2, 4, 7}th layers are convolutional layers with 256 filter and kernel size of 3×3 . The third and the sixth layers are rectified linear unit layers performing nonlinear feature mapping of $f_{\text{ReLU}}(x) = \max(0, x)$ for its input x . The fifth and the eighth layers are composed of pooling layers, which reduce the dimension by 2. There are fully connected layers, each of which is followed by a dropout layer with probability of 0.5, at the ninth and eleventh layers with 1024 units. The output layer is a classification layer with softmax function and P classes, each of which corresponds to a distinct subarray configuration.

IV. NUMERICAL EXPERIMENTS

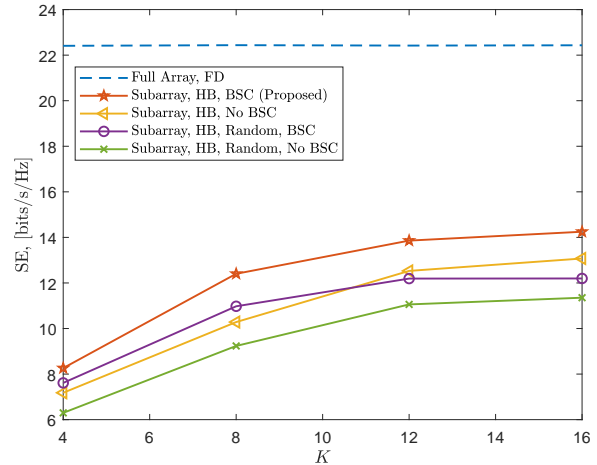
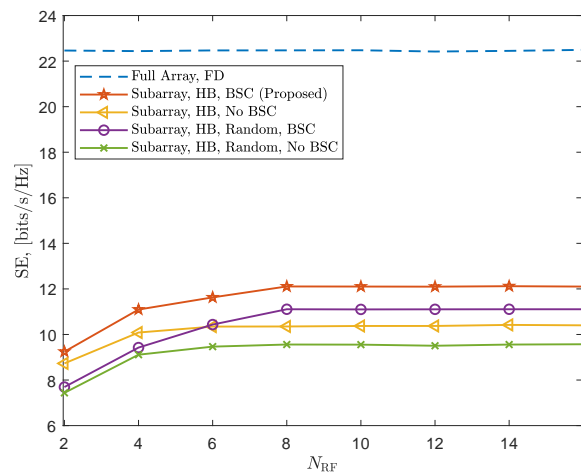
We evaluate the performance of the proposed approach via several experiments. During simulations, the target and user path directions are drawn uniform randomly as $\Phi_k, \phi_l, \theta_l \in [30^\circ, 150^\circ]$. We conducted 500 Monte Carlo trials, and presented the averaged results. We assumed that there are $T = 3$ point targets and a single user with $L = 3$ NLoS paths. We select $N' = 16$, $N_{\text{RF}} = 8$, $M = 16$ and the number of data snapshots $T_S = 256$.

Fig. 5 shows the SE performance of the proposed antenna selection and hybrid beamforming approach based on GSS and BSC for $N = 32$ and $N = 128$ when $K = 8$ and $G = 4$. The performance of the fully digital (FD) full array beamformer (i.e., $\bar{\mathbf{F}}_{\text{SC}}[m] = \varepsilon \bar{\mathbf{F}}_{\text{C}}[m] + (1 - \varepsilon) \bar{\mathbf{F}}_{\text{S}} \mathbf{D}[m]$) is regarded as benchmark for the subarrayed hybrid beamformer, i.e., $\mathbf{F}_{\text{RF}}^{(q^*)} \mathbf{F}_{\text{BB}}^{(q^*)}[m]$. The beamforming and antenna selection

(a) $N = 32, K = 8$ (b) $N = 128, K = 8$ Fig. 5. SE performance versus SNR for (a) $N = 32$ and (b) $N = 128$ when $K = 8, G = 4$ and $\varepsilon = 0.5$.

are performed as described in Algorithm 1 and Algorithm 2, respectively. We see from Fig. 5 that our BSC approach provides a significant SE improvement for hybrid beamforming. In order to evaluate the performance of antenna selection accuracy, we also present the hybrid beamforming performance of the randomly selected subarrays with and without BSC. While the former design involves a BSC beamformer for a random subarray configuration, the latter does not involve BSC for the same randomly selected subarray. We observed that the randomly selected beamformer with BSC performs better than that of optimized subarray without BSC for different array sizes. In other words, compensating for beam-squint plays more crucial role than optimizing for best subarray.

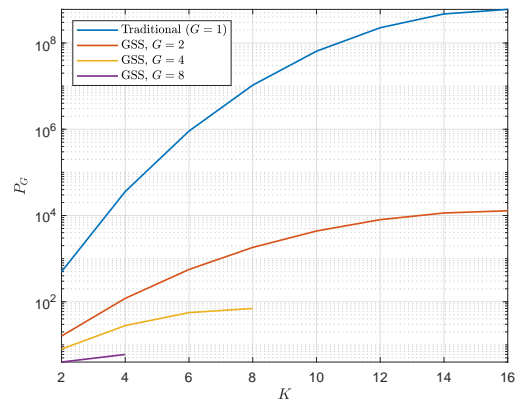
Next, we present the SE performance in Fig. 6 with respect to the number of selected antennas K when the transmit array size is fixed as $N = 64$ with $G = 4$. We aim to generate $T + L = 6$ disjoint beams towards $T = 3$ targets and $L = 3$ user path directions. Thus, we see that the SE is improved as K increases, especially for $K \geq T + L = 6$,

Fig. 6. SE versus number of selected antennas K when $N = 64, G = 4, \varepsilon = 0.5$ and $\text{SNR} = 0$ dB.Fig. 7. SE and number of RF chains when $N = 128, K = 8, G = 4, \varepsilon = 0.5$ and $\text{SNR} = 0$ dB.

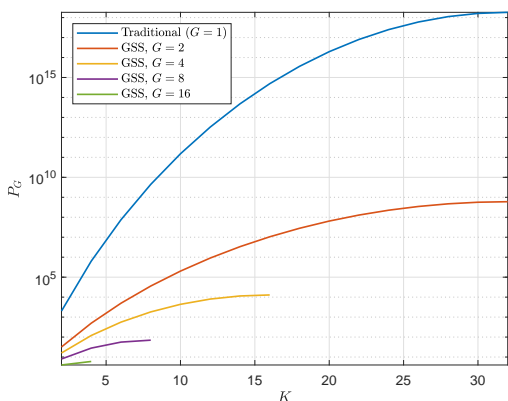
thanks to achieving higher beamforming gain. We also observe that optimized subarray without BSC achieves higher SE than the random subarray with BSC as $K \geq 10$. This suggests that implementing BSC in the case of the random subarray can improve the SE up to a certain extent. Furthermore, increasing the subarray size can potentially enhance the array gain, thereby mitigating the SE loss caused by beam-squint.

The SE performance is presented in Fig. 7 versus the number of RF chains N_{RF} for $N = 128$ and $K = 8$. As $N_{\text{RF}} \geq 6$, higher SE is achieved by the randomly selected subarray even without BSC. In contrast, the SE performance of the BSC algorithms is reduced for $N_{\text{RF}} < 8$. This is because the term $(\mathbf{F}_{\text{RF}}^{(q^*)})^\dagger \check{\mathbf{F}}_{\text{RF}}^{(q^*)}[m]$ in (28) becomes full column rank as $N_{\text{RF}} \rightarrow N$, hence provides a better mapping from $\check{\mathbf{F}}_{\text{BB}}^{(q^*)}[m]$ to $\mathbf{F}_{\text{BB}}^{(q^*)}[m]$. Nevertheless, our optimized subarray with BSC exhibits approximately 9% and 27% higher SE as compared to random subarray with and without BSC, respectively.

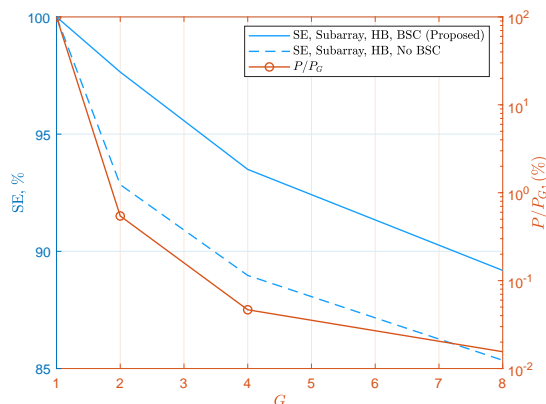
In Fig. 8, we evaluate the performance of our GSS approach



(a)



(b)



(c)

Fig. 8. Number of possible subarray configurations for traditional antenna selection and GSS when (a) $N = 32$ and (b) $N = 64$. (c) SE and number of subarray configurations versus G when $N = 16$, $K = 8$, $\varepsilon = 0.5$ and $\text{SNR} = 0$ dB.

in terms of number of subarray candidates as well as the loss in SE. Fig. 8(a-b) shows that the number of possible subarray configurations significantly reduces with the slight increase of G while the SE of the selected subarray degrades. This is because the antenna selection algorithm with GSS visits only the subarray configurations in \mathcal{Q}_G while leaving out the remaining candidates, which are in the set $\mathcal{Q} \setminus \mathcal{Q}_G$. Nevertheless, our

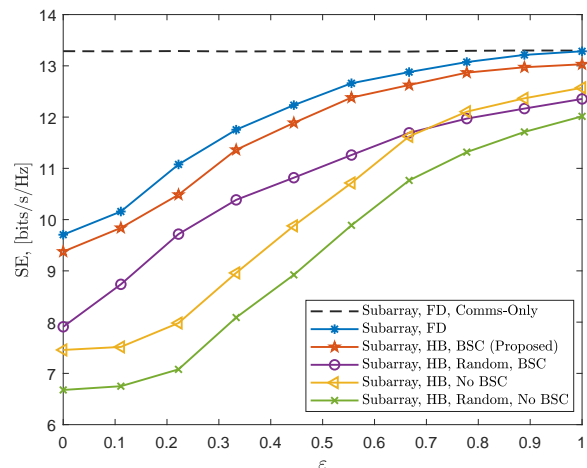
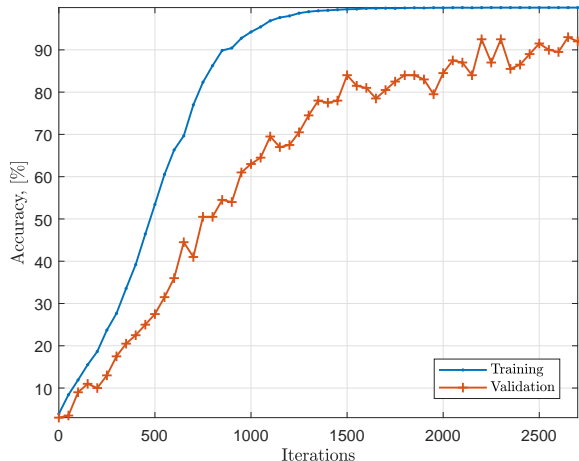


Fig. 9. SE versus trade-off parameter ε for $N = 32$, $K = 8$, $G = 4$ and $\text{SNR} = 0$ dB.

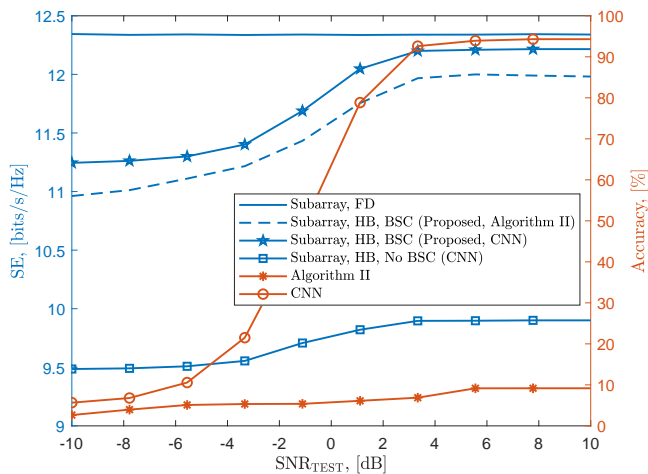
GSS approach with BSC-based hybrid beamforming achieves significantly low complexities while maintaining a satisfactory SE performance as shown in Fig. 8(c). In particular, when $G = 4$, the number of subarray candidates are reduced about 95% while our BSC approach yields only 6% loss in SE, whereas this loss is approximately 11% for the subarray beamforming without BSC.

The trade-off between communications and sensing is evaluated in Fig. 9 for $\varepsilon \in [0, 1]$, $N = 32$, $K = 8$, and $G = 4$. As a benchmark, the ISAC hybrid beamforming approach is also included with the FD communications-only beamformer (i.e., $\mathbf{F}_C^{(q^*)}[m]$) as well as the FD beamformer given in (18), which depends on ε . The FD ISAC beamformer attains the FD communications-only beamformer for $\varepsilon = 1$ as expected while its performance degrades as $\varepsilon \rightarrow 0$ as the trade-off becomes sensing-weighted. Furthermore, we observe that our beamformer with BSC closely follows the FD beamformer with significant improvement compared to beam-squint corrupted and randomly selected designs.

Now, we evaluate the performance of our CNN model for antenna selection. The training dataset \mathcal{D} is generated for $l_1 = 1000$ different data realizations, i.e., $\mathbf{\Pi}[m]$. Then, for each realized data sample, synthetic noise is added onto the input data in order to make the model robust against corruptions and imperfections [19, 72]. Specifically, $l_2 = 100$ noise realizations are obtained for three different SNR values as $\text{SNR}_{\text{TRAIN}} \in \{15, 20, 25\}$ dB. This process is repeated for each data realizations $i_1 = 1, \dots, l_1$ and $m = 1, \dots, M$ when $T = 3$, $N' = 16$, $N = 32$, $K = 8$ and $G = 4$. As a result, the whole dataset includes $l = l_1 \cdot l_2 \cdot M \cdot 3 = 480,000$ samples, each of which is of size $32 \times 19 \times 2$. The whole data set is divided into 30% and 70% two parts for validation and training, respectively. The validation dataset is then used for testing the CNN model after it is corrupted by synthetic noise with the SNR of SNR_{TEST} . Stochastic gradient descent algorithm with momentum of 0.9 is adopted during training, for which the cross-entropy loss function is used for classification



(a)



(b)

Fig. 10. Performance of the learning-based antenna selection. (a) training and validation accuracy during training. (b) SE performance versus SNR_{TEST} when $N = 32$, $K = 8$, $G = 4$ and $\varepsilon = 0.5$.

as

$$\text{ce} = -\frac{1}{I} \sum_{i=1}^I \sum_{p=1}^P \left(\omega_{i,p} \ln(\kappa_{i,p}) + (1 - \omega_{i,p}) \ln(1 - \kappa_{i,p}) \right)$$

where $\omega_{i,p}$ and $\kappa_{i,p}$ are the input-output pair of the classification layer defined for the i -th data sample and p -th class. The learning rate for training is set as 0.01 and it is reduced by half after each 500 iterations. The performance of the CNN model is presented in Fig. 10. Specifically, Fig. 10(a) shows the classification (subarray selection) accuracies for validation and training. We can see that the CNN model successfully learns the training data while the accuracy for validation data is slightly less with approximately 90% accuracy. This is because the validation data is not used during training. We also present the antenna selection accuracy and the SE performance of the selected subarrays after employing Algorithm 2 and CNN in Fig. 10(b). In this setup, the validation data is corrupted by synthetic noise defined by SNR_{TEST} in order to assess the

TABLE I
COMPUTATION TIMES (IN SECONDS)

	Model-based	Learning-based
$K = 2$	0.287	0.037
$K = 3$	1.876	0.037
$K = 4$	22.270	0.037
$K = 5$	67.946	0.037
$K = 6$	116.463	0.037
$K = 7$	184.378	0.037
$K = 8$	269.441	0.038

TABLE II
COMPUTATION TIMES (IN SECONDS) FOR SELECTING $K = 8$ OUT OF
 $N = 16$ ANTENNAS

	$G = 1$	$G = 2$	$G = 4$
Model-based	269.441	20.865	0.328
Learning-based	0.037	0.037	0.037

robustness of the proposed CNN model and Algorithm 2, for which the corrupted data (i.e., $\mathbf{\Pi}[m]$) is used as input, and the corresponding hybrid beamformers are estimated. Then, the true channel data is used to compute the SE with the resulting hybrid beamformers. Our CNN model achieves up to 95% antenna selection accuracy for the corrupted input data with 10 dB noise while the model-based approach in Algorithm 2 is unable to provide accurate antenna selection results (approximately 10%) due to the corruptions in the data. This observation clearly shows the advantage of using learning-models in imperfect scenarios. Specifically, the CNN accounts for the imperfections in the data and yields the accurate subarray selection performance thanks to training with noisy communications and sensing data for robustness. When we compare the SE of model-based and learning-based approaches (in the left axis), we can see that the corrupted input data causes selecting inaccurate subarray indices, thereby leading to poor SE performance. Nevertheless, CNN-based antenna selection yields (about 2%) higher SE than the model-based approach in Algorithm 2 in the presence of imperfect communications and sensing data.

Finally, we present the computation times (in seconds) for joint antenna selection and hybrid beamforming approach in Table I and Table II. In particular, Table I shows the computation times of model-based (Algorithm 2) and learning-based approaches for $K \in \{2, \dots, 8\}$, $N = 16$ and $G = 1$. While the complexity of the model-based approach grows geometrically, the learning-based approach with the CNN model in Fig. 4 enjoys significantly low computation times. The fast implementation of CNN is attributed to employing parallel processing tools e.g., graphical computation units (GPUs). We also present the computation times with respect to the group size G in Table II when $N = 16$ and $K = 8$. Note that the time complexity when $G = 1$ corresponds to the traditional antenna selection whereas $G > 1$ is for the proposed GSS strategy. The results are in accordance with Fig. 8 where a performance analysis with respect to P and G are presented. We see that our GSS approach approximately 11 and 630 times faster than traditional antenna selection for $G = 2$ and $G = 4$, respectively. Furthermore, the time complexity of

learning-based antenna selection with the CNN model exhibits approximately the same amount of time for $G \in \{1, 2, 4\}$ while providing a significant reduction (~ 7000 times faster) for computing the best subarray index as compared to the model-based approach.

V. SUMMARY

In this paper, we investigated the antenna selection problem in the presence of beam-squint for THz-ISAC hybrid beamforming. We have shown that the impact of beam-squint on antenna selection causes significant performance loss in terms of SE due to selecting inaccurate subarrays. The compensation for beam-squint during hybrid beamforming design is achieved via manifold optimization integrated with the proposed BSC algorithm. In particular, BSC provides a solution via updating the baseband beamformers by taking into account the distortions in the analog domain due to beam-squint. Specifically, BSC exhibits approximately 15% improvement in terms of SE without requiring additional hardware components. In order to solve the joint antenna selection and hybrid beamforming, low complexity algorithms are proposed to reduce the number of possible subarray configurations. These include sequential search algorithm to reduce the memory usage during the computation of the subarray variables and GSS to reduce the number of possible subarray configurations via selecting the antennas in small groups. It is shown that the proposed GSS approach provides approximately 95% reduction in terms of computational complexity while maintaining satisfactory performance with about 6% SE loss.

REFERENCES

- [1] F. Rusek, D. Persson, B. K. Lau, E. G. Larsson, T. L. Marzetta, O. Edfors, and F. Tufvesson, "Scaling Up MIMO: Opportunities and Challenges with Very Large Arrays," *IEEE Signal Process. Mag.*, vol. 30, no. 1, pp. 40–60, Dec. 2012.
- [2] K. V. Mishra, M. R. B. Shankar, V. Koivunen, B. Ottersten, and S. A. Vorobyov, "Toward millimeter-wave joint radar communications: A signal processing perspective," *IEEE Signal Process. Mag.*, vol. 36, no. 5, pp. 100–114, 2019.
- [3] R. W. Heath, N. González-Prelcic, S. Rangan, W. Roh, and A. M. Sayeed, "An overview of signal processing techniques for millimeter wave MIMO systems," *IEEE J. Sel. Top. Signal Process.*, vol. 10, no. 3, pp. 436–453, 2016.
- [4] A. M. Elbir, K. V. Mishra, S. Chatzinotas, and M. Bennis, "Terahertz-band integrated sensing and communications: Challenges and opportunities," *arXiv preprint arXiv:2208.01235*, 2022.
- [5] F. Liu, C. Masouros, A. P. Petropulu, H. Griffiths, and L. Hanzo, "Joint radar and communication design: Applications, state-of-the-art, and the road ahead," *IEEE Trans. Commun.*, vol. 68, no. 6, pp. 3834–3862, 2020.
- [6] A. M. Elbir, K. V. Mishra, and S. Chatzinotas, "Terahertz-band joint ultra-massive MIMO radar-communications: Model-based and model-free hybrid beamforming," *IEEE J. Sel. Top. Signal Process.*, vol. 15, no. 6, pp. 1468–1483, 2021.
- [7] J. A. Zhang, F. Liu, C. Masouros, R. W. Heath, Z. Feng, L. Zheng, and A. Petropulu, "An Overview of Signal Processing Techniques for Joint Communication and Radar Sensing," *IEEE J. Sel. Top. Signal Process.*, vol. 15, no. 6, pp. 1295–1315, Sep. 2021.
- [8] V. Petrov, G. Fodor, J. Kokkonen, D. Moltchanov, J. Lehtomaki, S. Andreev, Y. Koucheryavy, M. Juntti, and M. Valkama, "On Unified Vehicular Communications and Radar Sensing in Millimeter-Wave and Low Terahertz Bands," *IEEE Wireless Commun.*, vol. 26, no. 3, pp. 146–153, 2019.
- [9] J. Choi, V. Va, N. Gonzalez-Prelcic, R. Daniels, C. R. Bhat, and R. W. Heath, "Millimeter-Wave Vehicular Communication to Support Massive Automotive Sensing," *IEEE Commun. Mag.*, vol. 54, no. 12, pp. 160–167, Dec. 2016.
- [10] H. Wymeersch, A. Pärssinen, T. E. Abruđan, A. Wolfgang, K. Haneda, M. Sarajlic, M. E. Leinonen, M. F. Keskin, H. Chen, S. Lindberg, P. Kyösti, T. Svensson, and X. Yang, "6G Radio Requirements to Support Integrated Communication, Localization, and Sensing," in *2022 Joint European Conference on Networks and Communications & 6G Summit (EuCNC/6G Summit)*. IEEE, Jun. 2022, pp. 463–469.
- [11] Z. Chen, C. Han, Y. Wu, L. Li, C. Huang, Z. Zhang, G. Wang, and W. Tong, "Terahertz Wireless Communications for 2030 and Beyond: A Cutting-Edge Frontier," *IEEE Commun. Mag.*, vol. 59, no. 11, pp. 66–72, Nov. 2021.
- [12] Y. Cui, F. Liu, X. Jing, and J. Mu, "Integrating Sensing and Communications for Ubiquitous IoT: Applications, Trends, and Challenges," *IEEE Network*, vol. 35, no. 5, pp. 158–167, Nov. 2021.
- [13] C. Chaccour, M. N. Soorki, W. Saad, M. Bennis, P. Popovski, and M. Debbah, "Seven Defining Features of Terahertz (THz) Wireless Systems: A Fellowship of Communication and Sensing," *IEEE Commun. Surv. Tutorials*, vol. 24, no. 2, pp. 967–993, Jan. 2022.
- [14] B. Chang, W. Tang, X. Yan, X. Tong, and Z. Chen, "Integrated Scheduling of Sensing, Communication, and Control for mmWave/THz Communications in Cellular Connected UAV Networks," *IEEE J. Sel. Areas Commun.*, vol. 40, no. 7, pp. 2103–2113, 2022.
- [15] A. M. Elbir, K. V. Mishra, M. R. B. Shankar, and S. Chatzinotas, "The rise of intelligent reflecting surfaces in integrated sensing and communications paradigms," *IEEE Network*, pp. 1–8, 2022.
- [16] H. Sarrıeddeen, M.-S. Alouini, and T. Y. Al-Naffouri, "An overview of signal processing techniques for terahertz communications," *Proc. IEEE*, vol. 109, no. 10, pp. 1628–1665, 2021.
- [17] O. E. Ayach, S. Rajagopal, S. Abu-Surra, Z. Pi, and R. W. Heath, "Spatially sparse precoding in millimeter wave MIMO systems," *IEEE Trans. Wireless Commun.*, vol. 13, no. 3, pp. 1499–1513, 2014.
- [18] A. M. Elbir, K. V. Mishra, S. A. Vorobyov, and R. W. Heath, "Twenty-Five Years of Advances in Beamforming: From convex and nonconvex optimization to learning techniques," *IEEE Signal Process. Mag.*, vol. 40, no. 4, pp. 118–131, Jun. 2023.
- [19] A. M. Elbir and K. V. Mishra, "Joint antenna selection and hybrid beamformer design using unquantized and quantized deep learning networks," *IEEE Trans. Wireless Commun.*, vol. 19, no. 3, pp. 1677–1688, 2020.
- [20] Y. Gao, H. Vinck, and T. Kaiser, "Massive MIMO Antenna Selection: Switching Architectures, Capacity Bounds, and Optimal Antenna Selection Algorithms," *IEEE Trans. Signal Process.*, vol. 66, no. 5, pp. 1346–1360, Dec. 2017.
- [21] O. T. Demir and T. E. Tuncer, "Antenna Selection and Hybrid Beamforming for Simultaneous Wireless Information and Power Transfer in Multi-Group Multicasting Systems," *IEEE Trans. Wireless Commun.*, vol. 15, no. 10, pp. 6948–6962, Jul. 2016.
- [22] X. Wang, A. Hassanien, and M. G. Amin, "Dual-Function MIMO Radar Communications System Design Via Sparse Array Optimization," *IEEE Trans. Aerosp. Electron. Syst.*, vol. 55, no. 3, pp. 1213–1226, Aug. 2018.
- [23] R. Chen, R. W. Heath, and J. G. Andrews, "Transmit Selection Diversity for Unitary Precoded Multiuser Spatial Multiplexing Systems With Linear Receivers," *IEEE Trans. Signal Process.*, vol. 55, no. 3, pp. 1159–1171, Feb. 2007.
- [24] L. You, X. Qiang, C. G. Tsinos, F. Liu, W. Wang, X. Gao, and B. Ottersten, "Beam squint-aware integrated sensing and communications for hybrid massive MIMO LEO satellite systems," *IEEE J. Sel. Areas Commun.*, vol. 40, no. 10, pp. 2994–3009, 2022.
- [25] A. Alkhateeb and R. W. Heath, "Frequency selective hybrid precoding for limited feedback millimeter wave systems," *IEEE Trans. Commun.*, vol. 64, no. 5, pp. 1801–1818, 2016.
- [26] F. Shu, Y. Qin, T. Liu, L. Gui, Y. Zhang, J. Li, and Z. Han, "Low-complexity and high-resolution DOA estimation for hybrid analog and digital massive MIMO receive array," *IEEE Trans. Commun.*, vol. 66, no. 6, pp. 2487–2501, 2018.
- [27] A. M. Elbir, W. Shi, A. K. Papazafeiropoulos, P. Kourtessis, and S. Chatzinotas, "Terahertz-Band Channel and Beam Split Estimation via Array Perturbation Model," *IEEE Open J. Commun. Soc.*, vol. 4, pp. 892–907, Mar. 2023.
- [28] B. Wang, M. Jian, F. Gao, G. Y. Li, and H. Lin, "Beam squint and channel estimation for wideband mmWave massive MIMO-OFDM systems," *IEEE Trans. Signal Process.*, vol. 67, no. 23, pp. 5893–5908, 2019.
- [29] F. Gao, B. Wang, C. Xing, J. An, and G. Y. Li, "Wideband beamforming for hybrid massive MIMO terahertz communications," *IEEE J. Sel. Areas Commun.*, vol. 39, no. 6, pp. 1725–1740, 2021.

- [30] L. Dai, J. Tan, Z. Chen, and H. V. Poor, "Delay-phase precoding for wideband THz massive MIMO," *IEEE Trans. Wireless Commun.*, vol. 21, no. 9, pp. 7271–7286, 2022.
- [31] A. M. Elbir, K. V. Mishra, A. Abdallah, A. Celik, and A. M. Eltawil, "Spatial Path Index Modulation in mmWave/THz-Band Integrated Sensing and Communications," *arXiv*, Mar. 2023.
- [32] A. M. Elbir and S. Chatzinotas, "BSA-OMP: Beam-split-aware orthogonal matching pursuit for THz channel estimation," *IEEE Wireless Commun. Lett.*, p. 1, Feb. 2023.
- [33] A. M. Elbir, K. V. Mishra, A. Celik, and A. M. Eltawil, "Millimeter-Wave Radar Beamforming with Spatial Path Index Modulation Communications," in *2023 IEEE Radar Conference (RadarConf23)*. IEEE, May 2023, pp. 1–6.
- [34] A. M. Elbir, K. V. Mishra, and Y. C. Eldar, "Cognitive radar antenna selection via deep learning," *IET Radar, Sonar & Navigation*, vol. 13, pp. 871–880, 2019.
- [35] L. Wang, Q. He, and H. Li, "Transmitter selection and receiver placement for target parameter estimation in cooperative radar-communications system," *IET Signal Proc.*, vol. 16, no. 7, pp. 776–787, Sep. 2022.
- [36] Z. Xu, F. Liu, and A. Petropulu, "Cramér-Rao Bound and Antenna Selection Optimization for Dual Radar-Communication Design," in *ICASSP 2022 - 2022 IEEE International Conference on Acoustics, Speech and Signal Processing (ICASSP)*. IEEE, May 2022, pp. 5168–5172.
- [37] X. Wang, A. Hassanien, and M. G. Amin, "Sparse transmit array design for dual-function radar communications by antenna selection," *Digital Signal Process.*, vol. 83, pp. 223–234, Dec. 2018.
- [38] H. Huang, L. Wu, B. Shankar, and A. M. Zoubir, "Sparse Array Design for Dual-Function Radar-Communications System," *IEEE Commun. Lett.*, vol. 27, no. 5, pp. 1412–1416, Mar. 2023.
- [39] S. Sanayei and A. Nosratinia, "Capacity of MIMO Channels With Antenna Selection," *IEEE Trans. Inf. Theory*, vol. 53, no. 11, pp. 4356–4362, Oct. 2007.
- [40] S. Sanayei and A. Nosratinia, "Antenna selection in MIMO systems," *IEEE Commun. Mag.*, vol. 42, no. 10, pp. 68–73, Oct. 2004.
- [41] H. Godrich, A. P. Petropulu, and H. V. Poor, "Sensor Selection in Distributed Multiple-Radar Architectures for Localization: A Knapsack Problem Formulation," *IEEE Trans. Signal Process.*, vol. 60, no. 1, pp. 247–260, Sep. 2011.
- [42] X. Gao, O. Edfors, F. Tufvesson, and E. G. Larsson, "Massive MIMO in Real Propagation Environments: Do All Antennas Contribute Equally?" *IEEE Trans. Commun.*, vol. 63, no. 11, pp. 3917–3928, Jul. 2015.
- [43] L. Xu, S. Sun, Y. D. Zhang, and A. Petropulu, "Joint Antenna Selection and Beamforming in Integrated Automotive Radar Sensing-Communications with Quantized Double Phase Shifters," in *ICASSP 2023 - 2023 IEEE International Conference on Acoustics, Speech and Signal Processing (ICASSP)*. IEEE, Jun. 2023, pp. 1–5.
- [44] Z. Liu, Y. Yang, F. Gao, T. Zhou, and H. Ma, "Deep Unsupervised Learning for Joint Antenna Selection and Hybrid Beamforming," *IEEE Trans. Commun.*, vol. 70, no. 3, pp. 1697–1710, Jan. 2022.
- [45] T. X. Vu, S. Chatzinotas, V.-D. Nguyen, D. T. Hoang, D. N. Nguyen, M. Di Renzo, and B. Ottersten, "Machine Learning-Enabled Joint Antenna Selection and Precoding Design: From Offline Complexity to Online Performance," *IEEE Trans. Wireless Commun.*, vol. 20, no. 6, pp. 3710–3722, Jan. 2021.
- [46] S. Shrestha, X. Fu, and M. Hong, "Optimal Solutions for Joint Beamforming and Antenna Selection: From Branch and Bound to Graph Neural Imitation Learning," *IEEE Trans. Signal Process.*, vol. 71, pp. 831–846, Feb. 2023.
- [47] F. Liu and C. Masouros, "Hybrid beamforming with sub-arrayed MIMO radar: Enabling joint sensing and communication at mmWave band," in *IEEE International Conference on Acoustics, Speech and Signal Processing*, 2017, pp. 7770–7774.
- [48] I. F. Akyildiz, C. Han, Z. Hu, S. Nie, and J. M. Jornet, "Terahertz band communication: An old problem revisited and research directions for the next decade," *IEEE Trans. Commun.*, vol. 70, no. 6, pp. 4250–4285, 2022.
- [49] S. Ju and T. S. Rappaport, "140 GHz Urban Microcell Propagation Measurements for Spatial Consistency Modeling," in *ICC 2021 - IEEE International Conference on Communications*. IEEE, Jun. 2021, pp. 1–6.
- [50] S. Ju, Y. Xing, O. Kanhere, and T. S. Rappaport, "Sub-Terahertz Channel Measurements and Characterization in a Factory Building," in *ICC 2022 - IEEE International Conference on Communications*. IEEE, May 2022, pp. 2882–2887.
- [51] H. Yuan, N. Yang, K. Yang, C. Han, and J. An, "Hybrid beamforming for terahertz multi-carrier systems over frequency selective fading," *IEEE Trans. Commun.*, vol. 68, no. 10, pp. 6186–6199, 2020.
- [52] L. Yan, C. Han, and J. Yuan, "A Dynamic Array-of-Subarrays Architecture and Hybrid Precoding Algorithms for Terahertz Wireless Communications," *IEEE J. Sel. Areas Commun.*, vol. 38, no. 9, pp. 2041–2056, 2020.
- [53] A. M. Elbir, "A Unified Approach for Beam-Split Mitigation in Terahertz Wideband Hybrid Beamforming," *IEEE Trans. Veh. Technol.*, pp. 1–6, Apr. 2023.
- [54] K. Dovelos, M. Matthaiou, H. Q. Ngo, and B. Bellalta, "Channel estimation and hybrid combining for wideband terahertz massive MIMO systems," *IEEE J. Sel. Areas Commun.*, vol. 39, no. 6, pp. 1604–1620, 2021.
- [55] J. Tan and L. Dai, "Wideband channel estimation for THz massive MIMO," *China Commun.*, vol. 18, no. 5, pp. 66–80, May 2021.
- [56] E. Balevi and J. G. Andrews, "Wideband Channel Estimation With a Generative Adversarial Network," *IEEE Trans. Wireless Commun.*, vol. 20, no. 5, pp. 3049–3060, Jan. 2021.
- [57] A. F. Molisch, M. Z. Win, Y.-S. Choi, and J. H. Winters, "Capacity of MIMO systems with antenna selection," *IEEE Trans. Wireless Commun.*, vol. 4, no. 4, pp. 1759–1772, Jul. 2005.
- [58] X. Yu, G. Cui, J. Yang, L. Kong, and J. Li, "Wideband MIMO radar waveform design," *IEEE Trans. Signal Process.*, vol. 67, no. 13, pp. 3487–3501, 2019.
- [59] R. Schmidt, "Multiple emitter location and signal parameter estimation," *IEEE Trans. Antennas Propag.*, vol. 34, no. 3, pp. 276–280, 1986.
- [60] Y. Chen, L. Yan, C. Han, and M. Tao, "Millidegree-Level Direction-of-Arrival Estimation and Tracking for Terahertz Ultra-Massive MIMO Systems," *IEEE Trans. Wireless Commun.*, vol. 21, no. 2, pp. 869–883, Aug. 2021.
- [61] A. M. Elbir, "DeepMUSIC: Multiple signal classification via deep learning," *IEEE Sens. Lett.*, vol. 4, no. 4, pp. 1–4, 2020.
- [62] D. Fan, Y. Deng, F. Gao, Y. Liu, G. Wang, Z. Zhong, and A. Nallanathan, "Training Based DOA Estimation in Hybrid mmWave Massive MIMO Systems," in *GLOBECOM 2017 - 2017 IEEE Global Communications Conference*. IEEE, Dec. 2017, pp. 1–6.
- [63] A. R. Chiriyath, B. Paul, G. M. Jacyna, and D. W. Bliss, "Inner bounds on performance of radar and communications co-existence," *IEEE Trans. Signal Process.*, vol. 64, no. 2, pp. 464–474, 2015.
- [64] S. H. Dokhanchi, B. S. Mysore, K. V. Mishra, and B. Ottersten, "A mmWave automotive joint radar-communications system," *IEEE Trans. Aerosp. Electron. Syst.*, vol. 55, no. 3, pp. 1241–1260, 2019.
- [65] N. Boumal, B. Mishra, P.-A. Absil, and R. Sepulchre, "Manopt, a Matlab Toolbox for Optimization on Manifolds," *Journal of Machine Learning Research*, vol. 15, pp. 1455–1459, 2014. [Online]. Available: <http://jmlr.org/papers/v15/boumal14a.html>
- [66] X. Yu, J. Shen, J. Zhang, and K. B. Letaief, "Alternating Minimization Algorithms for Hybrid Precoding in Millimeter Wave MIMO Systems," *IEEE J. Sel. Topics Signal Process.*, vol. 10, no. 3, pp. 485–500, 2016.
- [67] L. Zhou, L. Zheng, X. Wang, W. Jiang, and W. Luo, "Coordinated Multicell Multicast Beamforming Based on Manifold Optimization," *IEEE Commun. Lett.*, vol. 21, no. 7, pp. 1673–1676, Apr. 2017.
- [68] J. Du, W. Xu, C. Zhao, and L. Vandendorpe, "Weighted Spectral Efficiency Optimization for Hybrid Beamforming in Multiuser Massive MIMO-OFDM Systems," *IEEE Trans. Veh. Technol.*, vol. 68, no. 10, pp. 9698–9712, Jul. 2019.
- [69] T. T. Truong and H.-T. Nguyen, "Backtracking Gradient Descent Method and Some Applications in Large Scale Optimisation. Part 2: Algorithms and Experiments," *Appl. Math. Optim.*, vol. 84, no. 3, pp. 2557–2586, Dec. 2021.
- [70] J. B. Andersen, "Array gain and capacity for known random channels with multiple element arrays at both ends," *IEEE J. Sel. Areas Commun.*, vol. 18, no. 11, pp. 2172–2178, Nov. 2000.
- [71] L. Zheng and D. N. C. Tse, "Diversity and multiplexing: a fundamental tradeoff in multiple-antenna channels," *IEEE Trans. Inf. Theory*, vol. 49, no. 5, pp. 1073–1096, May 2003.
- [72] A. M. Elbir, K. V. Mishra, M. R. B. Shankar, and B. Ottersten, "A family of deep learning architectures for channel estimation and hybrid beamforming in multi-carrier mm-Wave massive MIMO," *IEEE Trans. Cognit. Commun. Networking*, vol. 8, no. 2, pp. 642–656, 2021.